Mechanically Corner-Coupled Square Microresonator Array for Reduced Series Motional Resistance

Mustafa U. Demirci, *Member, IEEE*, and Clark T.-C. Nguyen, *Senior Member, IEEE*

Abstract—Substantial reductions in vibrating micromechanical resonator series motional resistance R_x have been attained by mechanically coupling and exciting a parallel array of corner-coupled polysilicon square plate resonators. Using this technique with seven resonators, an effective R_x of 480 Ω has been attained at 70 MHz, which is more than 5.9X smaller than the 2.82 kΩ exhibited by a stand-alone transverse-mode corner-supported square resonator, and all this achieved while still maintaining an effective $Q > 9000$. This method for R_x-reduction is superior to methods based on brute force scaling of electrode-to-resonator gaps or dc-bias increases, because it allows a reduction in R_x without sacrificing linearity, and thereby breaks the R_x versus dynamic range tradeoff often seen when scaling. This paper also compares two types of anchoring schemes for transverse-mode square micromechanical resonators and models the effect of support beam parameters on resonance frequency.   [1451]

Index Terms—Array, impedance, mechanical coupling, micromechanical resonator, motional resistance, quality factor, resonator, radio frequency (RF) microelectromechanical systems (MEMS), square plate.

I. INTRODUCTION

HAVING recently broken the GHz frequency "barrier" with Q's greater than 10,000 in both vacuum and air [1], vibrating micromechanical ("μ mechanical") resonators are emerging as viable candidates for on-chip versions of the high-Q resonators [e.g., quartz crystals, surface acoustic waves (SAW) resonators] used in wireless communication systems for frequency generation and filtering, with only a handful of issues left to solve [2]–[6]. Among the more important of the remaining issues that still hinder deployment of these devices in RF front ends is their larger-than-conventional impedance. In particular, it is their large impedance (i.e., motional resistance R_x) that presently prevents capacitively transduced vibrating micromechanical resonator devices in the VHF and UHF ranges from directly coupling to antennas in wireless communication

applications, where matching impedances in the range of 50 Ω and 377 Ω are often required.

Among the most direct methods for lowering the motional resistance R_x of capacitively transduced micromechanical resonators are: 1) scaling down the electrode-to-resonator gap [7]; 2) raising the dc-bias voltage; and 3) summing together the outputs of an array of identical resonators [8]. Unfortunately, each of these methods comes with drawbacks. In particular, although the first two are very effective in lowering R_x, with fourth power and square law dependencies, respectively, they do so at the cost of linearity [10]. On the other hand, method (3) actually improves linearity while lowering R_x. Unfortunately, as will be described, method (3) is difficult to implement, since it requires resonators with precisely identical responses—a tough bill when Q's are as large as exhibited by micromechanical resonators.

This paper presents a method for lowering motional resistance based on method (3), with all of its linearity advantages, but dispensing with the need to match the responses of high-Q resonators by mechanically coupling them so that they automatically generate a single resonance response (i.e., mode) where all resonators vibrate at precisely the same frequency. Using this technique with seven strategically-designed, corner-coupled square resonators (demonstrated for the first time), an effective R_x of 480 Ω has been attained at 70 MHz, which is more than 5.9X smaller than the 2.82 kΩ exhibited by a stand-alone transverse-mode corner-supported square resonator, and all this achieved while still maintaining an effective $Q > 9000$. This method for R_x-reduction is superior to methods based on scaling of electrode-to-resonator gaps or dc-bias increases, because it allows a reduction in R_x without sacrificing linearity [10], and thereby breaks the R_x versus dynamic range tradeoff associated with "brute force" scaling.

II. SQUARE PLATE MICROMECHANICAL RESONATOR

Pursuant to realizing reductions in R_x via mechanically coupled parallel resonator arrays, a new transverse-mode square plate resonator, shown in Fig. 1, was strategically designed to allow for greater flexibility in the relative phasings between input and output signals during operation—something that will be needed to specify the array output frequency. The device consists of a square plate suspended from 90–180 nm (specified by fabrication process) above four triangular capacitive transducer electrodes, with an anchor at its center. The electrodes are independently accessible (for phase flexibility) and identical in size for symmetry in electrostatic force distribution and topography. They are centered at antinode locations for maximum efficacy, and are separated by diagonal leads that pass through the anchor
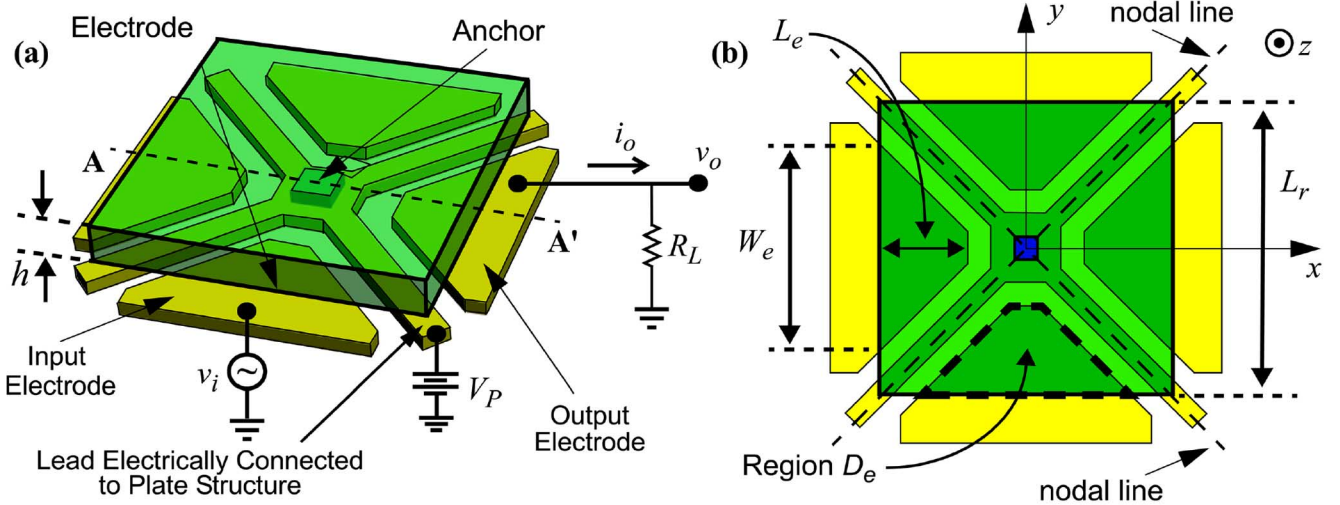
Fig. 1. (a) Perspective-view schematic of a square plate μ resonator in a two-port excitation configuration. (b) Top-view schematic identifying the axes and dimensions.

and provide an electrical connection to the plate. As the structure carries a dc-potential, the leads serve as a ground shield between input and output electrodes.

The electrical operation of the structure is similar to that of previous capacitively transduced microresonators [1], [5], [7]. An ac voltage v_i applied to the input electrode generates an electrostatic actuation force which is amplified by the dc-bias voltage V_P applied to the resonator structure via the diagonal leads. The induced vibration at resonance results in a time-varying dc-biased capacitor between the output electrode and the square plate, which in turn produces an output current $i_o = V_P(\partial C/\partial z)(\partial z/\partial t)$, where $\partial C/\partial z$ is the unit change in electrode-to-resonator overlap capacitance per z-directed change in gap spacing.

As seen in the ANSYS-simulated symmetric transverse-mode shape for this device in Fig. 2, the anchor at the center of the device corresponds to an effective motionless node point at which vertical energy losses to the substrate are minimized due to momentum cancellation in the bulk of the device, resulting in higher Q for this device, hence, better stand-alone R_x than a clamped-clamped beam. The vibration is purely torsional (i.e., no vertical motion) along the two nodal lines which are indicated in Fig. 1(b).

A. Resonance Characteristics

The nominal resonance frequency f_{nom} for a square plate vibrating in the mode of Fig. 2 is given by [11]

$$f_{\text{nom}} = 0.9697 \sqrt{\frac{E}{\rho}} \frac{h}{L_r^2} \qquad (1)$$

where h is the structure thickness, L_ρ is the side length of the plate, and E, ρ, and ν are the Young's modulus, density, and Poisson ratio, respectively, of its structural material. Note that (1) represents the mechanical resonance frequency of the plate
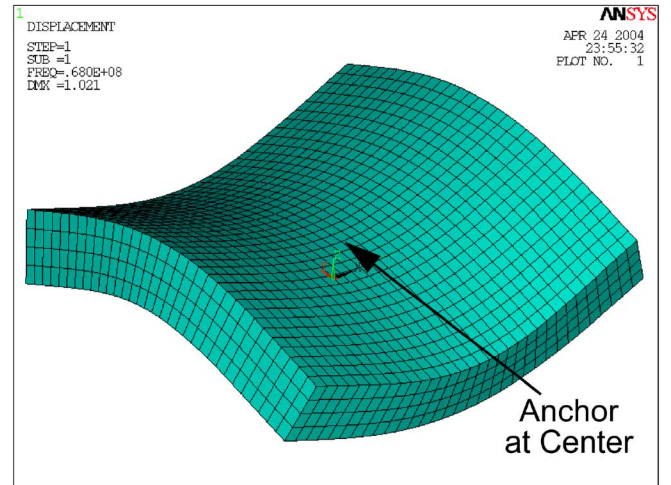

Fig. 2. Transverse vibration mode shape of a square plate simulated via ANSYS.

when there are no applied voltages (i.e., no electromechanical coupling). If the effect of electromechanical coupling is included, then the frequency equation takes on the form [7]

$$f_o = f_{\text{nom}} \left[1 - \left\langle \frac{k_e}{k_m} \right\rangle \right]^{1/2} \qquad (2)$$

where variable f_o represents the resonance frequency including the effect of the electromechanical coupling and $\langle k_e/k_m \rangle$ is a parameter representing the effective electrical-to-mechanical stiffness ratio integrated over the electrodes, given by

$$\left\langle \frac{k_e}{k_m} \right\rangle = N_e \int \int_{D_e} \frac{V_P^2 \varepsilon}{(d(x,y))^3 \, k_m(x,y)} dx dy \qquad (3)$$

where ϵ is the permittivity in the gap, $d(x,y)$ is the electrode-to-resonator gap spacing which varies as a function of location

(x, y) on the resonator plate due to V_P-derived forces that statically deflect the plate [7], [12], N_e is the total number of electrodes at a different potential than the resonator structure, D_e is the region of overlap of the square plate with its electrode as shown in Fig. 1(b), $k_m(x, y)$ is the vertical stiffness without electromechanical coupling (i.e., $V_P = 0$) at a location (x, y) on the square plate, given by [7]

$$k_m(x, y) = [2\pi f_{\mathrm{nom}}]^2 m_r(x, y) \qquad (4)$$

where $m_r(x, y)$ is the equivalent mass as a function of location (x, y), and the axes and all other geometric variables are as indicated in Fig. 1. The expression for the equivalent mass of the square plate resonator at a given point can be obtained from the total kinetic energy of the square plate divided by one-half of the squared velocity at that point as follows [13]:

$$m_r(x, y) = \frac{KE_{\mathrm{tot}}}{\frac{1}{2}[\nu(x, y)]^2}$$
$$= \frac{\frac{1}{2}\int_{-L_r/2}^{L_r/2}\int_{-L_r/2}^{L_r/2} \rho h [\nu(x', y')]^2\, dx'\, dy'}{\frac{1}{2}[\nu(x, y)]^2} \qquad (5)$$

where $\nu(x, y)$ is the velocity of the vibration in $+z$-direction at location (x, y) given in phasor form by

$$V(x, y) = \dot{Z}(x, y) = j\omega_o \kappa Z_{\mathrm{mode}}(x, y) \qquad (6)$$

where κ is a scaling constant, and $Z_{\mathrm{mode}}(x, y)$ is the mode shape of the device, which can be approximated by [14]

$$Z_{\mathrm{mode}}(x, y) = \cos\left(\frac{\pi x}{2L_r}\right) \cos\left(\frac{3\pi y}{2L_r}\right)$$
$$- \cos\left(\frac{3\pi x}{2L_r}\right) \cos\left(\frac{\pi y}{2L_r}\right). \qquad (7)$$

Using (6) and (7) in (5), the equivalent mass in the z-direction for a transverse-mode square plate becomes

$$m_r(x, y) = \frac{\rho h \int_{-L_r/2}^{L_r/2}\int_{-L_r/2}^{L_r/2} [Z_{\mathrm{mode}}(x', y')]^2\, dx'\, dy'}{[Z_{\mathrm{mode}}(x, y)]^2}. \qquad (8)$$

B. Phase Flexibility and Equivalent Circuit

The placement of the electrodes of the square plate resonator is such that each electrode resides in a triangular region between the two nodal lines to provide the optimum configuration to excite the vibration mode of Fig. 2. Because of the symmetry of the mode shape, the resonator is capable of generating output currents having $0°$ and $180°$ phase difference with the input voltage simultaneously via the excitation configuration of Fig. 3(a). At resonance, due to the difference in the directions of
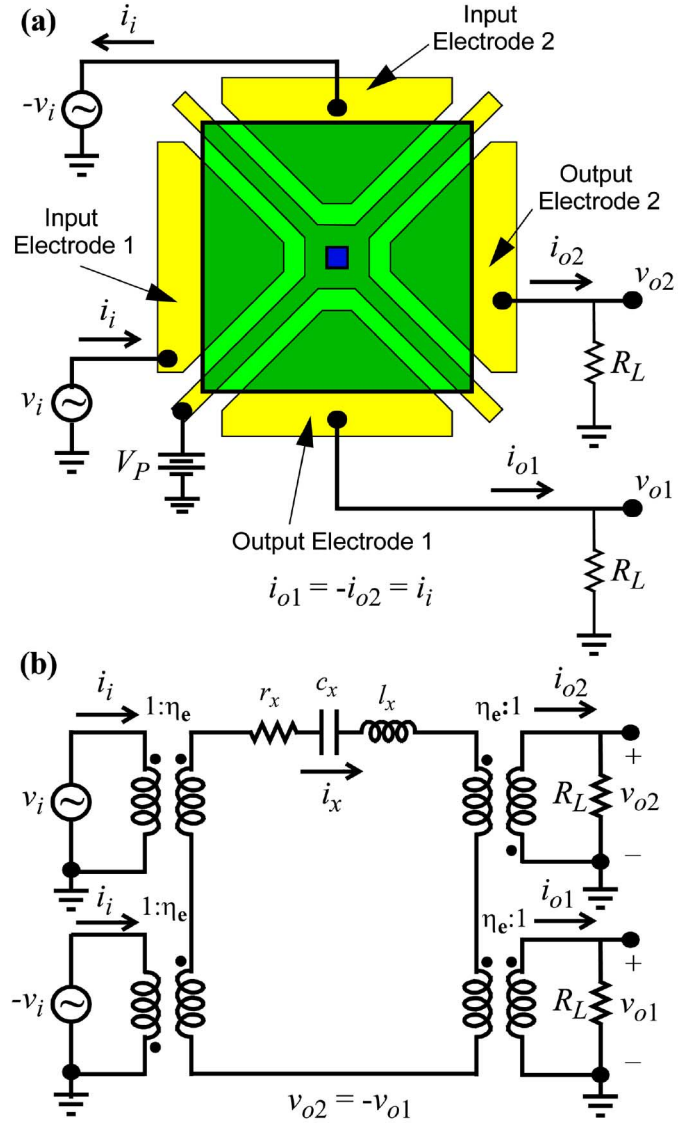

Fig. 3. (a) Top-view schematic of a square plate resonator in an excitation configuration to achieve two out-of-phase output signals with equal magnitudes. (b) Its equivalent circuit model.

vibration above the electrodes, the input and first output signal of the device are in phase (i.e., the output current i_{o_1} is equal to the input current i_i), while the input and second output signal are out-of-phase (i.e., i_{o_2} is equal to $-i_i$). Note that, although the first and second output signals have a $180°$ phase difference, they are equal in magnitude as the displacement amplitudes above each electrode are same. This phase flexibility can simplify the design of circuits, especially in oscillator and filter applications, where fully balanced excitation and detection can often be employed to null out parasitic feedthrough currents.

Fig. 3(b) presents the physically consistent *LCR* equivalent circuit for the device of Fig. 3(a), obtained via an impedance analysis similar to that previously applied to clamped-clamped beam resonators in [7]. This particular equivalent circuit is deemed "physically consistent" because the values of its circuit elements and transformers are derived directly from the

lumped mass, stiffness, damping, and voltage-to-force transfer function, of the mechanical device, and can be expressed as

$$l_x = m_{re} \quad c_x = \frac{1}{k_{re}} \quad r_x = \frac{\sqrt{k_{re}m_{re}}}{Q} = c_{re} \qquad (9)$$

where k_{re}, m_{re}, and c_{re}, are the effective stiffness, mass, and damping, respectively, at the highest velocity point of the square plate, obtained by evaluating

$$m_{re} = m_r \left(\frac{L_r}{2}, 0 \right) \quad k_{re} = k_r \left(\frac{L_r}{2}, 0 \right) \qquad (10)$$

where $k_r(x,y)$ is the effective system stiffness of the resonator, which differs from k_m in (4) in that it includes the influence of electromechanical coupling (i.e., of applied electrical bias). As with k_m, $k_r(x,y)$ is related to $m_r(x,y)$ via frequency, but this time via the bias-dependent radian resonance frequency ω_o as follows:

$$k_r(x,y) = \omega_o^2 m_r(x,y). \qquad (11)$$

In the physically consistent model of Fig. 3(b), the transformer turns ratio is simply given by the electromechanical coupling factor

$$\eta_e = V_P \frac{\partial C}{\partial z} \qquad (12)$$

which is identical for all (identical) ports. The change in resonator-to-electrode capacitance per unit displacement $\partial C/\partial z$ is given by

$$\frac{\partial C}{\partial z} = \left[\int \int_{D_e} \int \int_{D_e} \frac{Z_{\mathrm{mode}}(x,y)}{Z_{\mathrm{mode}}(x',y')} \cdot \frac{\varepsilon^2 k_{re} dx' dy' dx dy}{\left[d(x',y') d(x,y) \right]^2 \left[k_r(x',y') \right]} \right]^{1/2}. \qquad (13)$$

In practice, the complexity of the expression for dc-bias-induced static plate bending of the square resonator $d(x,y)$ often precludes convergence of (13) when evaluated via computer. Fortunately, the use of the complete form of $d(x,y)$ is often not necessary, as substitution of $d(x,y)$ with the static d_o yields sufficiently accurate results, as will be verified later in Section VI.

With all other ports grounded, the effective electrical impedance seen looking into a given port can be obtained by reflecting the *lcr* through the transformer at that port, to yield

$$L_x = \frac{m_{re}}{\eta_e^2} \quad C_x = \frac{\eta_e^2}{k_{re}} \quad R_x = \frac{c_{re}}{\eta_e^2}. \qquad (14)$$

Of the elements in (14), the series motional resistance R_x is the most influential in both oscillator and filter circuits. In oscillators [15], [16], R_x generally governs the gain needed to instigate and sustain oscillation; whereas in bandpass filters [7], it
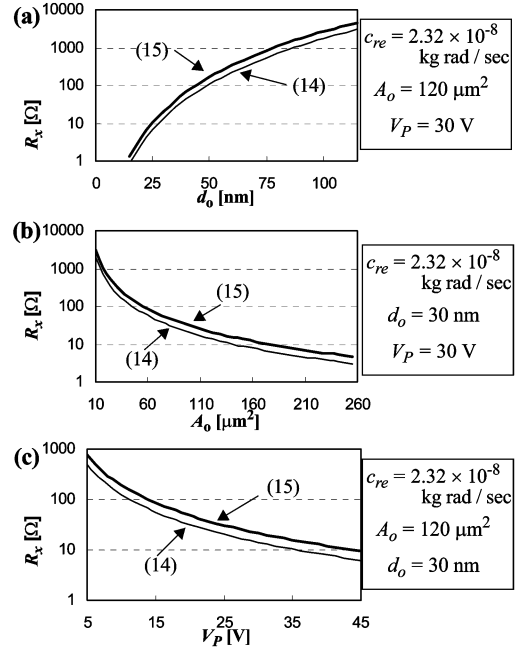

Fig. 4. Simulated plots comparing R_x values obtained via (14) and (15). (a) R_x versus electrode-to-resonator gap spacing d_o. (b) R_x versus electrode-to-resonator overlap area A_o. (c) R_x versus dc-bias V_P.

dictates the ease by which a given filter design can match to low impedance stages before and after the filter (e.g., the antenna).

III. R_x VERSUS LINEARITY

Pursuant to obtaining better insight into what parameters govern R_x, a less accurate, but more intuitive, closed form expression for R_x can be obtained by neglecting the bending and distributed stiffness modeled in (13) and just using static or lumped terms for integrated parameters, which yields

$$R_x = \frac{c_{re} d_o^4}{\varepsilon^2 A_o^2 V_P^2} \qquad (15)$$

where A_o is the effective electrode-to-resonator overlap area of the resonator, and Q is absorbed into c_{re}, given by (9). From (15), for a given Q, R_x can be lowered by decreasing the electrode-to-resonator gap spacing d_o, increasing the dc-bias V_P, increasing the permittivity ϵ, or increasing the overlap area A_o.

Fig. 4 presents plots of R_x versus various parameters in (15), using both (14) and (15) showing that values on the order of 10 Ω are in fact feasible if sufficiently small values of electrode-to-resonator gap spacing d_o and large values of dc-bias V_P are used. However, the use of such values comes at the price of linearity, as manifested in an increase in third-order intermodulation distorion (IM_3).

Third-order intermodulation distortion (IM_3) for a frequency filter occurs when system nonlinearities allow out-of-band signal components (tones) spaced from an in-band frequency ω_o by $\Delta\omega$ and $2\Delta\omega$, respectively, to generate an
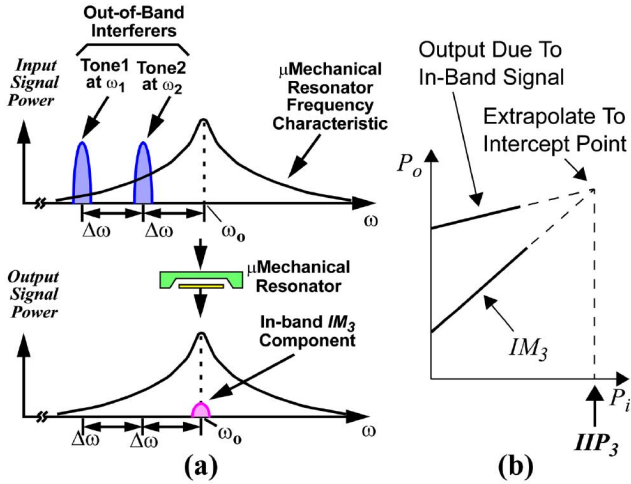
Fig. 5. (a) Schematic description of the different input and output signals of importance during an IIP_3 measurement. (b) P_o versus P_i plots during an IIP_3 measurement, showing how their intersection determines the intercept point.

in-band component S_{IM3} back at ω_o [9]. This phenomenon can be illustrated quantitatively by applying an input containing the desired signal (i.e., the fundamental) plus the two out-of-band (interfering) tones, given by

$$S_{in} = S_i \underbrace{[\cos \omega_o t}_{\text{Fundamental}} + \underbrace{\cos \omega_1 t}_{\text{Tone 1}} + \underbrace{\cos \omega_2 t]}_{\text{Tone 2}} \quad (16)$$

to the general nonlinear transfer function

$$S_{\text{out}} = A_o + A_1 S_{in} + A_2 S_{in}^2 + A_3 S_{in}^3 + \cdots \quad (17)$$

where $A_o, \ldots, A_n$ are constants if the system is memoryless. Inserting (16) into (17), then expanding, yields (among other components) (18),

$$S_{\text{out}} = \cdots + \underbrace{A_1 S_i \cos \omega_o t}_{\text{Fundamental}} + \underbrace{\tfrac{3}{4} A_3 S_i^3 \cos(2\omega_1 - \omega_2)}_{3^{\text{rd}}\text{-Order Intermod}(IM_3)} + \cdots \quad (18)$$

where an IM_3 component is seen to be generated via third-order nonlinearity represented by A_3.

For the common case where the interferers are located at frequencies $\Delta\omega$ and $2\Delta\omega$ from the fundamental [as shown in Fig. 5(a)], the quantity $(2\omega_1 - \omega_2)$ will be equal to ω_o, and the IM_3 component will be at the same frequency as the fundamental, possibly masking it if either A_3 or the interfering tone magnitudes are too large. In effect, as also illustrated in Fig. 5(a), even though the interfering tones are outside the filter passband, they still generate an in-band response—a highly undesirable situation for a filtering device designed to reject out-of-band signals. To suppress this effect, the third-order nonlinear term in (17) must be constrained below a minimum acceptable value in practical communication systems. Among the more useful metrics to gauge the ability of a system to suppress IM_3 distortion is the third-order input intercept point IIP_3, defined as the

input amplitude S_i at which the extrapolated IM_3 and fundamental output components are equal in magnitude, as shown in Fig. 5(b). In general, a large IIP_3 is preferred for communication applications.

From [10], the voltage V_{IIP3} and power P_{IIP3} at the third-order input intercept point IIP_3 for a capacitively driven square-plate micromechanical resonator are given to first order by

$$V_{IIP3} = \left\{ \frac{1}{4} \frac{\varepsilon A_o}{d_o^3} \frac{1}{k_{re}} [2\Theta_1 + \Theta_2^*] \right.$$
$$+ \frac{3}{4} \frac{(\varepsilon A_o)^2}{d_o^6} \frac{V_P^2}{k_{re}^2} \Theta_1 [\Theta_1 + 2\Theta_2^*]$$
$$\left. + \frac{3}{2} \frac{(\varepsilon A_o)^3}{d_o^9} \frac{V_P^4}{k_{re}^3} \Theta_1^2 \Theta_2^* \right\}^{-1/2} \quad (19)$$

$$P_{IIP3} = 10\text{Log} \left(\frac{V_{IIP3}^2}{R_S + R_x + R_L} \right) \quad (20)$$

where R_S and R_L are the source and load resistances surrounding the resonator during practical operation, $\Theta_1 = \Theta(\omega_1)$, and $\Theta_2 = \Theta(\omega_2)$, where

$$\Theta(\omega) = \frac{1}{1 - \left(\frac{\omega}{\omega_o}\right)^2 + \frac{j\omega}{(Q\omega_o)}}. \quad (21)$$

Here, the variables Θ_1, and Θ_2 model the degree to which the resonator's amplitude transfer function attenuates input tones at ω_1 and ω_2, respectively.

Inserting (19) into (20) and assuming that $R_x \gg R_S$ or R_L (which is the case, here), a compact expression for P_{IIP3} can be written as the "parallel" combination of several IM_3 power terms

$$P_{IIP3} = [P_{V^2X} \| P_{VX^2} \| P_{X^3}] \quad (22)$$

where P_{V^2X} and P_{VX^2} are terms emanating from nonlinear voltage and displacement interactions, given by

$$P_{V^2X} = \frac{2\omega_o Q V_P^2 \varepsilon A_o}{d_o [2\Theta_1 + \Theta_2]} \quad (23)$$

$$P_{VX^2} = \frac{2}{3} \frac{\omega_o Q d_o^2 k_{re}}{\Theta_1 [\Theta_1 + 2\Theta_2]} \quad (24)$$

and P_{X^3} derives from purely nonlinear displacement interactions, and is given by

$$P_{X^3} = \frac{\omega_o Q d_o^5 k_{re}^2}{3\varepsilon A_o V_P^2 \Theta_1^2 \Theta_2}. \quad (25)$$

Each of the previous terms competes to constrain the P_{IIP3}, and each will surface as the dominant constraint over different $(d_o, V_P, \epsilon, A_o)$ parameter spaces. For example, for large values of d_o, the P_{V^2X} term is often the smallest of the three terms, so dominates over the other terms to constrain the P_{IIP3}. In this case, one might raise the V_P, ϵ, or A_o, to attain a sufficiently large P_{IIP3}. However, as these variables are raised, the P_{X^3} term decreases and eventually becomes the dominant term, limiting the degree to which increases in these terms can improve
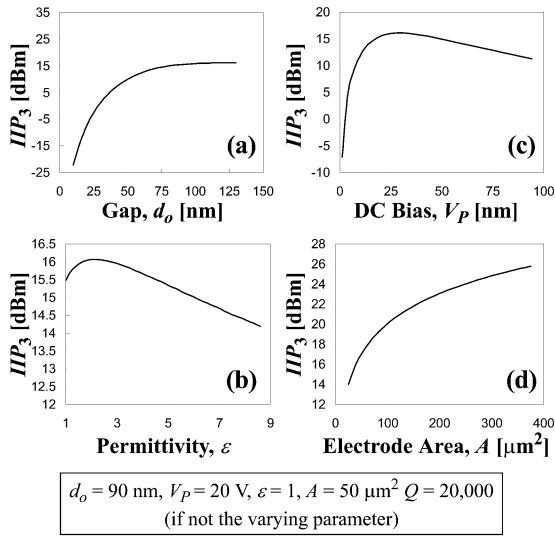
Fig. 6. Theoretical plots of $IIP3$ power versus (a) electrode-to-resonator gap spacing (d_o), (b) DC bias (V_P), (c) relative permittivity (ϵ), and (d) electrode area (A_o) for a square plate microresonator. Note that in (d), the effective resonator stiffness k_{re} is increased in proportion to the electrode area.

linearity. In fact, once the term becomes dominant, increases in these parameters only serve to degrade the P_{IIP3}. Thus, as illustrated in the plots of Fig. 6, there are ranges over which increases in different terms raise or lower the P_{IIP3}.

As already mentioned, the series motional resistance R_x can be manipulated by making changes to each of the parameters of Fig. 6. In particular, it can be lowered by decreasing d_o, or raising any of V_P, ϵ, or A_o. Of these options, only increasing the electrode-to-resonator overlap area A_o allows improvements over the entire range in the plot of Fig. 6(d), and in all three power terms (23)–(25), as it is increased. (Note that the A_o in the denominator of (25) cancels with that in k_{re}, leaving a net A_o in the numerator.) Thus, for a given capacitively transduced micromechanical resonator, often the best strategy for decreasing R_x with the least impact on linearity (and actually, with an improvement) is to increase the electrode-to-resonator overlap area.

As will be seen, this is exactly the approach taken when arraying the resonators of this work.

IV. CORNER-SUPPORTED SQUARE PLATE RESONATOR

In order to minimize anchor induced losses that can degrade Q, the resonator of Fig. 1(a) is anchored at the center, which is the intersection point of the nodal lines of its mode shape, hence a node point. Quality factors of devices anchored in this way are sensitive to misalignments between structure and the anchor. Self-aligned processes such as that of [1] are good solutions to prevent misalignment; however, they require extra steps, which can increase manufacturing cost. For applications where high quality factors are required, but a simple process flow is desired, Fig. 7 presents a square plate resonator with an alternative support scheme. Here, instead of a center stem, torsional mode beams attached at its nodal corners hold the resonator, in a scheme that now resembles more the support structure of free-free beam μmechanical resonators [17]. The beams connect to the corner of the plate at one end and anchor to the substrate at the other. Each beam extends along one of the nodal lines
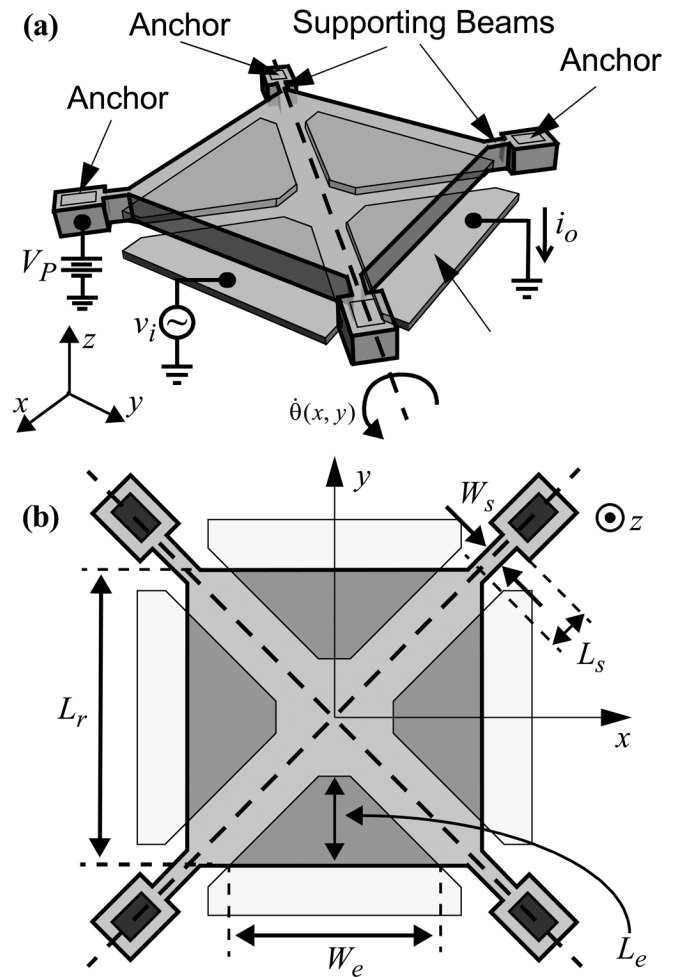

Fig. 7. (a) Perspective-view schematic of a corner-supported square plate μ resonator in a two-port bias and excitation configuration. (b) Top-view schematic.

of Fig. 7(b), where the vibration is only in torsion, so matches with the torsional motion of the support beam, allowing operation with minimal distortion to the resonator mode shape. As the device has anchors at its corners, the diagonal leads between the electrodes used in the design of Fig. 1 are no longer necessary for dc-bias access to the resonator plate. Removal of the diagonal leads leaves more area for signal electrodes, but has the drawback of increased input-to-output cross-talk. Another benefit of the corner-supported plate of Fig. 7 is that it is stiffer, so has a higher catastrophic pull-in voltage [18] than the center-stem device of Fig. 1, which allows a smaller series motional resistance R_x in cases where large dc-bias voltages can be accommodated.

Fig. 8 presents the ANSYS-simulated vibration mode shape of this device, which clearly shows that the supports do not appreciably distort the mode. However, they do cause an increase in the total stiffness of the resonator resulting in a resonance frequency greater than predicted by (1). To formulate the amount of increase in the frequency, one must consider the mass and stiffness addition introduced by the support beam. Since the vibration of the resonator is purely torsional along its nodal lines (i.e., diagonals of the plate), it is most convenient to work with torsional variables in this analysis. The angular velocity $\dot{\theta}(x, y)$ of the plate about the first nodal line [i.e., about the $y = x$ line,
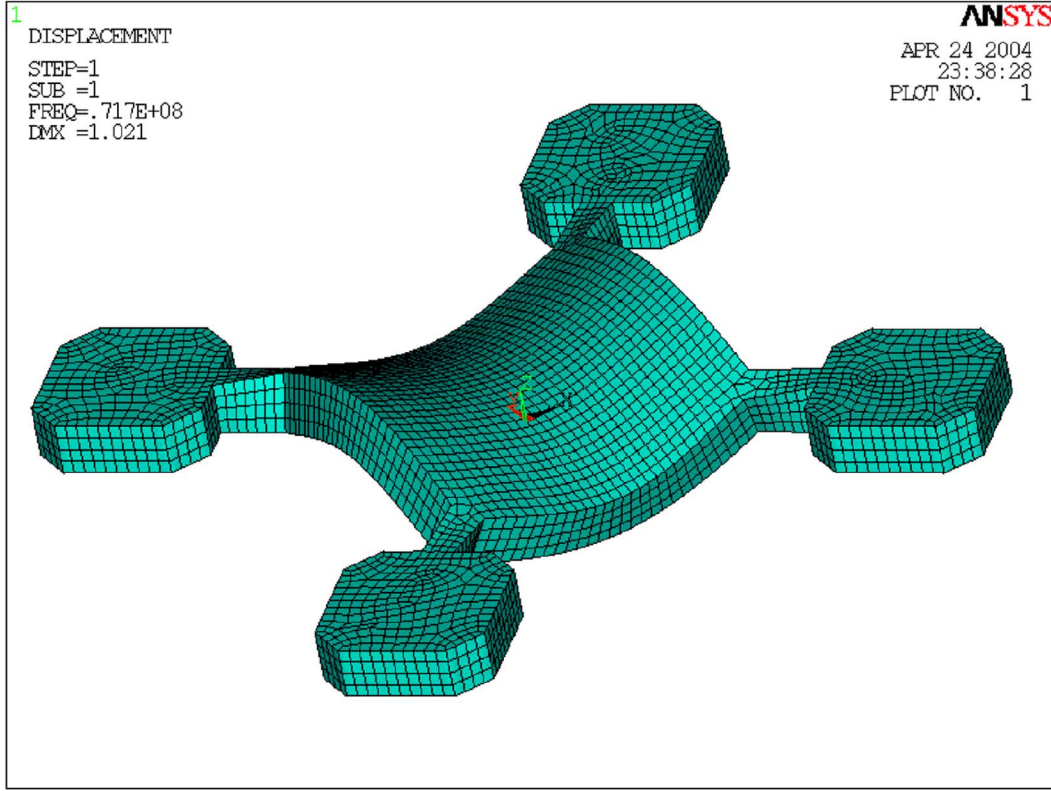
Fig. 8. Vibration mode shape of a square plate supported by torsional beams at corners as simulated via ANSYS.

as indicated in Fig. 7(a)] at location (x, y) is equal to the time derivative of the angle $\theta(x, y)$, which is related to the slope of the displacement $z(x, y)$ in the direction of the second nodal line (i.e., along the $y = -x$ line) as

$$\tan(\theta(x, y)) \cong \theta(x, y) = D_u z(x, y) \quad (26)$$

where $D_u z(x, y)$ is the directional derivative of the vertical displacement $z(x, y)$ in the direction of the unit vector $\bar{u} = (1, -1)$ and the approximation is valid since the displacement of the plate is small compared to the plate dimensions. As the time derivative of $z(x, y)$ is equal to the vertical velocity $v_z(x, y)$, the angular velocity is given by

$$\dot{\theta}(x, y) = D_u \nu_z(x, y)$$
$$= \frac{\partial}{\partial x} \nu_z(x, y) \cos\left(-\frac{\pi}{4}\right)$$
$$+ \frac{\partial}{\partial y} \nu_z(x, y) \sin\left(-\frac{\pi}{4}\right). \quad (27)$$

Thus, the equivalent resonator mass moment of inertia at location (x, y) along the first nodal line is [13]

$$J_{r\theta}(x, y) = \frac{KE_{\text{tot}}}{\left(\frac{1}{2}\right)(\dot{\theta}(x, y))^2}$$
$$= \frac{2\rho h \int_{-L_r/2}^{L_r/2} \int_{-L_r/2}^{L_r/2} [Z_{\text{mode}}(x', y')]^2 dx' dy'}{\left[\frac{\partial}{\partial x} Z_{\text{mode}}(x, y) - \frac{\partial}{\partial y} Z_{\text{mode}}(x, y)\right]^2} \quad (28)$$

and the rotational stiffness of the resonator along the nodal line then follows as [11]:

$$k_{r\theta}(x, y) = \omega_o^2 J_{r\theta}(x, y). \quad (29)$$

The mass moment of inertia and torsional stiffness of the support beam can be modeled by its equivalent acoustic T network model using the current analogy, where force is the across variable and velocity is the through variable [13]. For the case where the support beam length is smaller than half of an effective quarter-wavelength (or $\lambda/8$) of the resonator operating frequency—which is the case used for this work, since shorter support beams allow higher catastrophic pull-in voltages, in turn allowing higher dc-bias voltages V_P and lower motional resistances R_x—the acoustic T network takes the form shown in Fig. 9, where shunt and series arm impedances are modeled by reciprocal torsional stiffness $1/k_{s_\theta}$ and mass moment of inertia J_{s_θ}, respectively. The anchoring at one side of the support beam corresponds to an open circuit, leaving a series arm with circuit parameters $1/k_{s_\theta}$ and J_{s_θ}, given by

$$k_{s\theta} = \frac{G\gamma}{L_s} \quad J_{s\theta} = \frac{\rho J_s L_s}{2} \quad (30)$$

where G and J_s are the shear modulus of elasticity and polar moment of inertia, respectively, given by

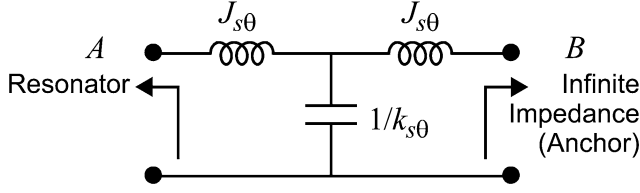$$G = \frac{E}{2(1+\nu)} \quad J_s = hW_s \frac{(h^2 + W_s^2)}{12} \quad (31)$$

Fig. 9. Equivalent acoustic T-network model for a short support beam ($L_s < \lambda/8$) that is attached to the resonator at port A and to the anchor at port B. This model also applies to coupling beams.
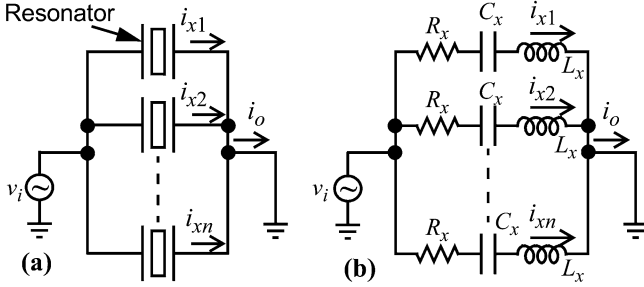

Fig. 10. (a) Array of resonators in parallel, each with motional resistance R_x, where n is the number of resonators in the array. (b) Equivalent LCR circuit.

and γ is the torsion constant [19], given for the case of rectangular cross section with $h/W_s = 1.6$ by

$$\gamma = 0.204hW_s^3. \tag{32}$$

The resonance frequency of a square plate suspended by short support beams, taking into account the mass moment of inertia and stiffness additions from the supports, is then given by

$$f_{nomS} = \frac{1}{2\pi} \left(\frac{k_{r\theta}\left(\frac{L_r}{2}, \frac{L_r}{2}\right) + 4k_{s\theta}}{J_{r\theta}\left(\frac{L_r}{2}, \frac{L_r}{2}\right) + 4J_{s\theta}} \right)^{1/2}. \tag{33}$$

It should be noted that this equation is only a first order approximation since it ignores the mass of the small portion at the intersection point of the plate and the support beam. Still, the equation gives good insight on the effect of support beam length on resonance frequency.

In the presence of a dc-bias V_P, the resonance frequency of a square plate suspended by short support beams is influenced by the effect of electromechanical coupling (i.e., by electrical stiffness), so takes on the form

$$f_{oS} = f_{nomS} \left[1 - \left\langle \frac{k_e}{k_m} \right\rangle \right]^{1/2}. \tag{34}$$

V. Coupled Microresonator Array

Again, the basic method for lowering motional resistance R_x in this work entails the summing of currents from several
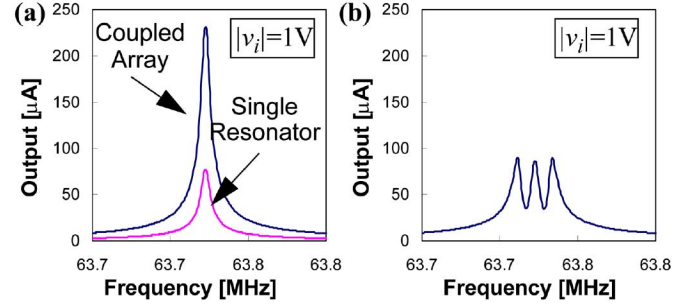

Fig. 11. Simulated frequency spectra showing (a) the increase in output attained by electrically coupling three identical square resonators, each with exactly the same frequency; and (b) the effect of a 0.01% mismatch in resonator frequencies.

resonators to produce a larger total current. Fig. 10 presents schematics depicting an electrically connected version of such an approach, where n resonators with identical frequency responses are connected in parallel and driven by a common input source v_i, with their motional currents summed by wired connections. In the ideal case, where all n resonators are held to exactly the same resonance frequency, this method can work well to increase the total current i_o through the resonator array by n times for the same input voltage v_i, hence lowering the effective motional resistance R_x by the same factor n. In equation form, assuming identical resonators, the equivalent motional resistance of the array is given by

$$R_{x\text{ARRAY}} = \frac{v_i}{i_o} = \frac{v_i}{n i_{x1}} = \frac{R_x}{n}. \tag{35}$$

From a parameter perspective, when a number n of these resonators are coupled into an array, the overall effective electrode area increases by a factor of n. From (22)–(25) in Section III, since an increase in the electrode-to-resonator overlap area A_o always leads to an increase in power at the third-order input intercept point P_{IIP3}, this arraying strategy reduces series motional resistance R_x without degrading linearity. This is in contrast to other available approaches to lowering R_x, such as reducing the electrode-to-resonator gap spacing d_o, raising the effective permittivity ϵ, or raising the dc-bias V_P, all of which eventually begin to degrade the $IIP3$.

Fig. 11(a) illustrates the increase in peak height (or improvement in R_x and power handling) attained when the outputs of three resonators, each with Q's of 20,000, are combined in this fashion. Unfortunately, this result is obtained only with the utmost control to match resonance frequencies, and even a tiny deviation in frequency from a matched case can dramatically compromise the combined output, as illustrated in Fig. 11(b), where resonator frequencies are mismatched by a mere 0.01%. Evidently, successful implementation of summation-based R_x-lowering in this electrically-connected fashion ultimately requires spacious and power hungry feedback control electronics to insure that the resonance frequencies of all resonators remain identical. Needless to say, this is not practical in scenarios where large numbers of resonators are needed in portable
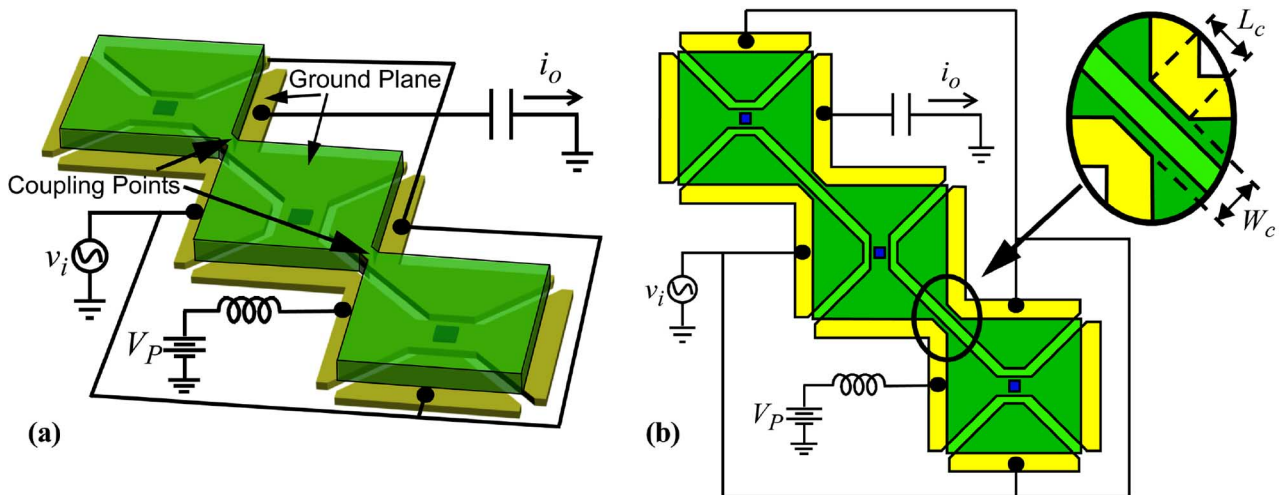
Fig. 12. (a) Perspective view and (b) top-view schematic of mechanically coupled array of three square resonators in a bias and excitation configuration that specifically selects the first filter mode. Note that the ground plane connects to all structures and is used for the output.
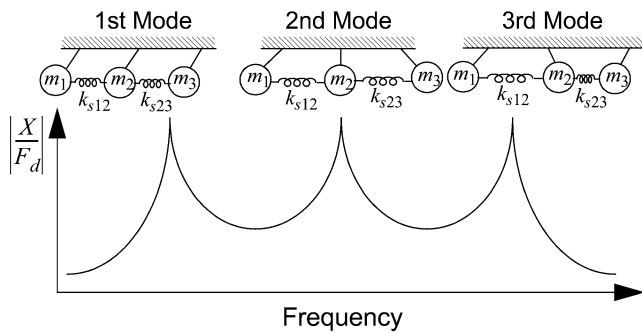

Fig. 13. Frequency spectrum showing the amplitude of each mode and phase relationships between resonators in each mode for a mechanically coupled array of three resonators.

applications, such as in RF channel-select receiver architectures [6].

Fortunately, mechanical coupling offers a superior solution to this resonator matching problem. In particular, by coupling the n resonators mechanically, as shown for square plate resonators in Fig. 12, a mechanical filter structure is achieved, which now exhibits n modal frequencies, where each mode corresponds to a specific frequency and mode shape, as illustrated in Fig. 13[20], [21]. When the overall filter structure vibrates at a given modal frequency, *all* coupled resonators (at least those that move in the given mode shape) vibrate at this same frequency—a very convenient phenomenon considering the problem at hand. Obtaining the desired single resonator response then amounts to designing the drive electrode configuration of the mechanically coupled resonator array system such that one of its modes is emphasized, while all others are suppressed.

Given this goal, it is advantageous to first separate the modes as far apart as possible. Since the bandwidth of a mechanical filter is proportional to the stiffness of its resonator-to-resonator coupling springs [7], [20], the first step in selecting a single mode, while suppressing others, is to couple the resonators with very stiff springs. (This in sharp contrast to the requirement for small percent bandwidth mechanical filters, which normally require fairly compliant springs.) Stiff mechanical coupling is
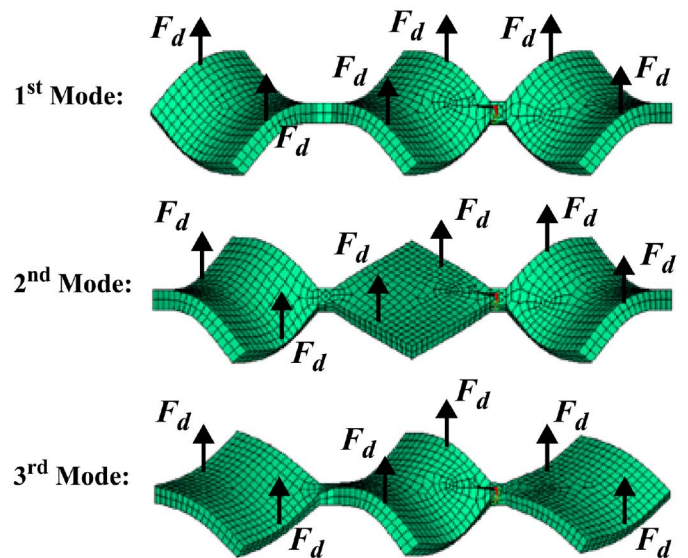

Fig. 14. ANSYS simulated filter mode shapes for the coupled three-resonator array of Fig. 12, with magnitude and directions for the electrostatic drive forces F_d induced by the hookup in Fig. 12.

achieved in Fig. 12 by coupling the square resonators right at their corners via short, stiff stubs.

Pursuant to accentuating one mode, while suppressing others, Fig. 13 shows that each mode in a given filter is distinguished from another by the relative phasings between its resonators. Thus, unwanted filter modes can be suppressed by imposing properly phased ac forces on constituent resonators that emphasize phasings associated with a desired mode shape, while counteracting all others. In this regard, the phase flexibility by which the constituent resonators in a mechanically coupled resonator array can be driven and sensed is key to selecting a single mode, and the availability of four different electrodes underneath the square resonators used for this work greatly facilitates the selection of a single mode. The input voltage connections shown in Fig. 12 are in fact chosen to accentuate the lowest frequency mode.
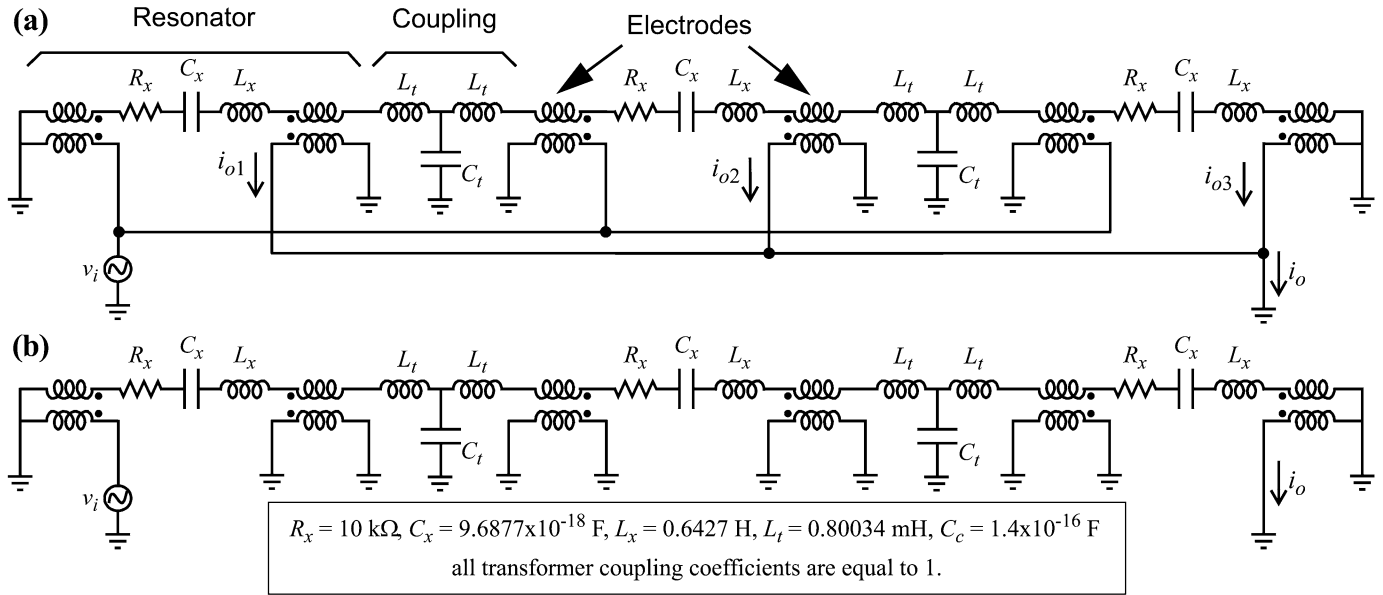
Fig. 15. Equivalent LCR circuit of a mechanically coupled three resonator array when operated (a) in the excitation configuration of Fig. 12 and (b) as a micromechanical filter. The given circuit element values are used in the simulations in Fig. 16.

To illustrate the manner by which properly phased forcing signals can accentuate the lowest mode, while suppressing all others, Fig. 14 places the force distribution generated by the electrode hookup of Fig. 12 over ANSYS simulations of the shapes of each of the three modes. Note how the force directions F_d imposed by the electrode connection of Fig. 12 all go in the same direction as the mode shape displacements for the first mode. Note also how this same force configuration opposes at least one of the mode shape displacements for each of the other modes, resulting in their suppression.

The resonance frequency of the first mode of the array in Fig. 14 is given in terms of constituent resonator mass and stiffnesses by

$$f_{o,\text{ARRAY}} = \frac{1}{2\pi}\sqrt{\frac{\sum_{i=1}^{N} k_{ri}}{\sum_{i=1}^{N} m_{ri} + \sum_{j=1}^{N} m_{sj}}} \qquad (36)$$

where k_{ri} and m_{ri} are the effective stiffness and mass, respectively, of the ith resonator; m_{sj} is the effective mass of the jth coupling stub; and where the resonance frequency of the ith constituent resonator is given by

$$f_{oi} = \frac{1}{2\pi}\sqrt{\frac{k_{ri}}{m_{ri}}}. \qquad (37)$$

If there is a slight change in the resonance frequency of any of the constituent resonators of the array (i.e., a slight change in k_{ri} or m_{ri}), this will cause a much smaller shift in the array resonance frequency, as it is averaged over N resonators. However, the resonators will still be vibrating in unison at the same frequency, as they are mechanically coupled. The frequency shift will also cause slight distortion in the mode shapes, which may result in inadequate mode suppression and hence spurious responses. However, as will be verified in Section VI, the amount

of this amplitude mismatch seems to be small enough that the spurious responses are not detectable—at least not by the measurement methods used here.

Although the array method should work for any strength of mechanical coupling, it is advantageous to use stiff coupling for two main reasons.

1) To make sure that if the undesired modes cannot be sufficiently suppressed, any spurious outputs they cause will be as far as possible from the chosen mode.
2) To prevent any resonance localization effects that may be possible for a sufficiently large number of weakly coupled structures [22].

Fig. 15(a) presents the equivalent *LCR* circuit representing the mechanically coupled array structure of Fig. 12 with the design and electrical biases summarized in Table I. Here, each identical resonator is modeled by an (identical) equivalent circuit of the form of Fig. 3, where the transformers modeling each port (i.e., each electrode) can be clearly seen. These circuits, however, differ from Fig. 3 in that the transformers have all been normalized to have 1:1 turns ratios, for ease of circuit analysis. To affect this normalization, the *lcr* element values in Fig. 3 must themselves be transformed through the electromechanical coupling turns ratio η_e to yield

$$L_x = \frac{l_x}{\eta_e^2}$$
$$C_x = \eta_e^2 c_x$$
$$R_x = \frac{r_x}{\eta_e^2} \qquad (38)$$

which are more in line with the actual electrical impedance seen looking into the device input and output terminals.

In Fig. 15, the corner couplers are modeled by *LC* equivalent T-networks, the values of which are determined by fitting the frequencies of the three modes obtained by simulating the *LCR* model to match the ANSYS simulated frequencies.

Parameter	Value	Unit
Square Plate Side Length, L_r	16	μm
Plate Thickness, h	2.1	μm
Electrode Width, W_e	14.6	μm
Electrode Length, L_e	5	μm
Coupling Beam Length, L_c	1.4	μm
Coupling Beam Width, W_c	1.4	μm
Resonator-to-Electrode Gap, d_o	180	nm
DC Bias, V_P	52	V
Input AC Voltage Amplitude, $|v_i|$	1	V
Resonator Quality Factor, Q	25,000	—

Fig. 17. Final cross section of a surface micromachined square plate microresonator (cross section taken along AA' in Fig. 1).
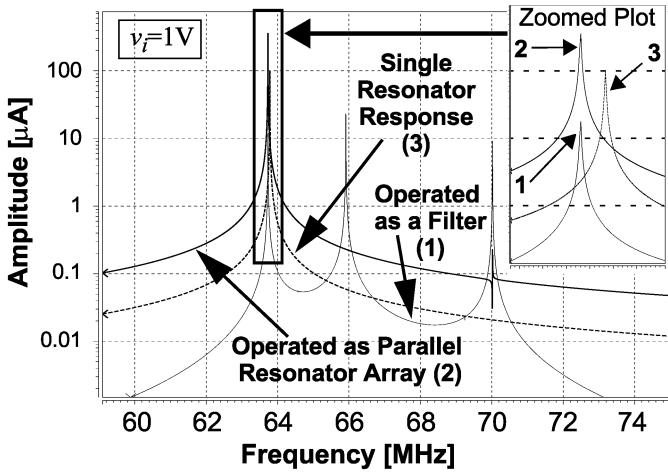

Fig. 16. SPICE simulated spectra for the structure of Fig. 12 when operated as a mechanical filter [circuit of Fig. 15(b)] and a parallel resonator array [circuit of Fig. 15(a)], all compared with the response of a single resonator (dashed line). Note that the amplitude-axis of the zoomed plot corresponds to the amplitude-axis of the main plot.

Fig. 16 presents SPICE simulated spectra for the equivalent circuit of the coupled structure for three cases

1) the structure operated as a parallel resonator array, using the hookup of Fig. 12, modeled by the circuit of Fig. 15(a);
2) the structure operated as an unterminated mechanical filter, with v_i applied to one end resonator, and i_o taken at the other end, all modeled by the circuit of Fig. 15(b);
3) a single stand-alone constituent resonator.

In the simulated plot for the mechanical filter of case 2), three distinct peaks are observed as expected, each of which correspond to the modes of Fig. 14. Unlike previous filters designed for small, specific bandwidths [7], [20], the peaks for case 2) are a few MHz apart from each other, as governed by the use of stiff mechanical couplers in this structure. The electrode-configuration of the parallel array in case 1), on the other hand, effectively suppresses the second and third mode peaks, while raising the output current at the single desired lowest mode frequency (which is the first mode in Fig. 14), by more than 9 dB—all as previously advertised.

As illustrated in Fig. 16, the first mode of the coupled structure does not exactly match the frequency of a stand-alone constituent resonator,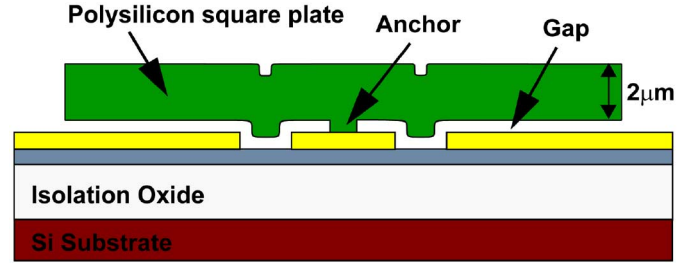 although its frequency is very close. Should a more exact match to the frequency of a stand-alone resonator be required, note that the modes are quite predictable by the models presented and, thus, can be set to any needed frequency by design.

VI. EXPERIMENTAL RESULTS

Stand-alone, center-stem, and corner-supported micromechanical square plate resonators and mechanically-coupled arrays of them with resonance frequencies between 60 and 72 MHz were designed using the theory in Sections II, IV, and V and fabricated in a four-mask polysilicon surface micromachining technology, similar to previously reported versions [7]. Fig. 17 presents the final cross-section of the fabrication process for a center-anchored square plate. The resonators constituting the arrays were designed identical to stand-alone resonators in all dimensions to allow an accurate comparison of motional resistances. Also, all the coupling stubs in the arrays of this paper are identical and have a length (L_c) and width (W_c) of 1.4 μm.

Table II summarizes the 68-MHz center-stem, and 72-MHz corner-supported square plate designs of this paper. Figs. 18 and 19 present SEMs of a fabricated 68-MHz single center-stem square resonator and mechanically-coupled array of three of them, respectively. Figs. 20 and 21 present the SEM's of a fabricated 72-MHz stand alone corner-supported square resonator and a mechanically-coupled array of seven of them.

For measurement and characterization, each resonator die was mounted on a printed circuit board and placed in a custom-built vacuum chamber. DC and coaxial feedthroughs through a grounded metal block, which served as one of the vacuum chamber walls, provided electrical access to the circuit board. A turbomolecular vacuum pump provided operating pressures down to 200 μTorr, where viscous gas damping [24] is greatly suppressed, allowing resonators under test to exhibit their maximum Q's. Devices were measured using an HP 8751A network analyzer and S-parameter test set.

A. Stand-Alone Square Plate Resonators

Fig. 22 presents the frequency spectrum for a center-stem square plate resonator with 16 μm-sides measured under vacuum using the one-port test setup [26] shown in the figure inset and a dc-bias voltage of 25 V. As shown, this device exhibits a Q of 15,000 at 68.5 MHz, which is on par with free-free beam resonator Q's [25] at the same frequency. Its series motional resistance R_x extracted from the plot is 13.4 kΩ. It should be noted that although this device is perhaps best operated as a two-port, it is being operated as a one-port here for

TABLE II
SQUARE PLATE RESONATOR DESIGN AND PERFORMANCE SUMMARY

| Parameter | Resonator Type | | | Unit |
	Center-Stem (Fig. 1)	Center-Stem (Fig. 1)	Corner-Support (Fig. 7)	
Target Frequency	68	68	72	MHz
Square Plate Side Length, L_r	16	16	16	μm
Support Beam Length, L_s	—	—	2.5	μm
Support Beam Width, W_s	—	—	1.4	μm
Measured Plate Thickness, h	2.2	2.2	2.2	μm
Effective Plate Thickness, h_{eff}	2.243	2.230	2.243	μm
Electrode Width, W_c	10	10	10	μm
Electrode Length, L_e	4	4	4.5	μm
Resonator-to-Electrode Gap, d_o (measured)	90	90	90	nm
Res.-to-Electrode Gap, d_o (extrapolated via ((13))) **	96	98	86	nm
Young's Modulus, E	150	150	150	GPa
Poisson Ratio, ν ([23])	0.226	0.226	0.226	—
Quality Factor, Q	15,000	10,500	17,500	—
DC Bias, V_{Pm}	25	20	40	V
Pull-in Voltage (measured)	29	25	45	V
Resonance Frequency, f_o (measured)	68.49	68.15	71.69	MHz
Frequency, f_o ($V_P=V_{Pm}$) (calculated via ((2)))***	68.50	68.15	68.26	MHz
Frequency, f_{nom} ($V_P=0$V) (calculated via ((1)))***	68.60	68.21	68.60	MHz
Frequency (with Supports), f_{oS} ($V_P=V_{Pm}$) (calculated via ((34)))***	—	—	71.34	MHz
Motional Resistance, R_x (measured)	13.4	32.3	2.82	kΩ
Motional Resistance, R_x (calculated via Eq. ((9)))*	13.5	32.4	2.84	kΩ

* $d(x,y) = d_o$ assumed in this calculation.
**   Really more a first order approximation to $d(x,y)$ than a value for the static d_o.
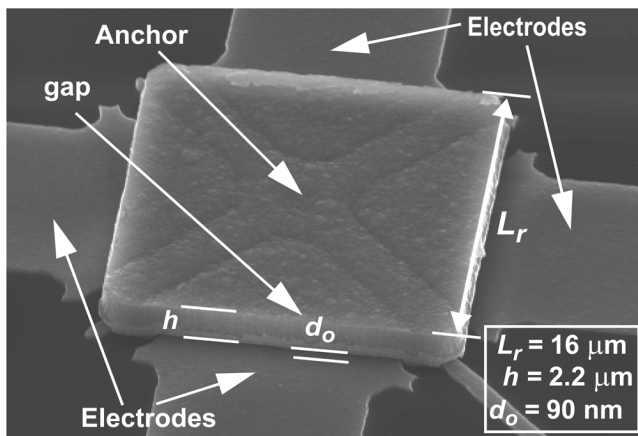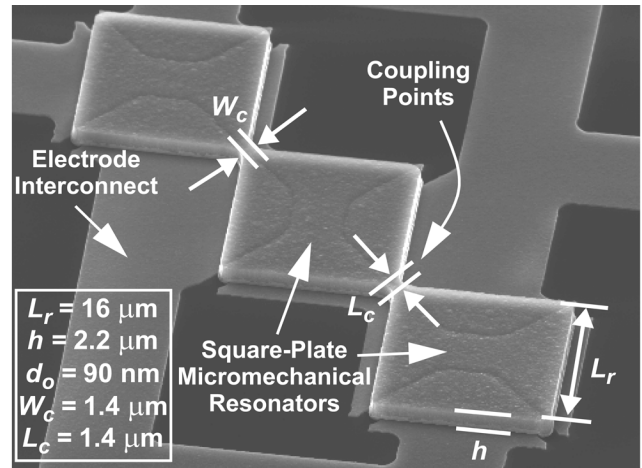*** $h = h_{eff}$ assumed in this calculation.

Fig. 19. SEM of a 68-MHz mechanically coupled array of three center-stem square plate resonators.

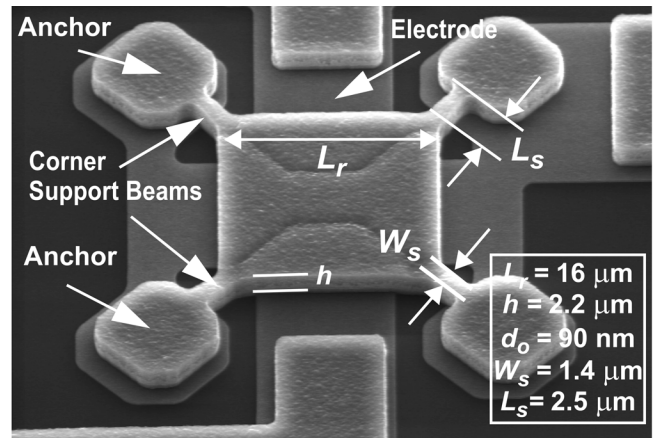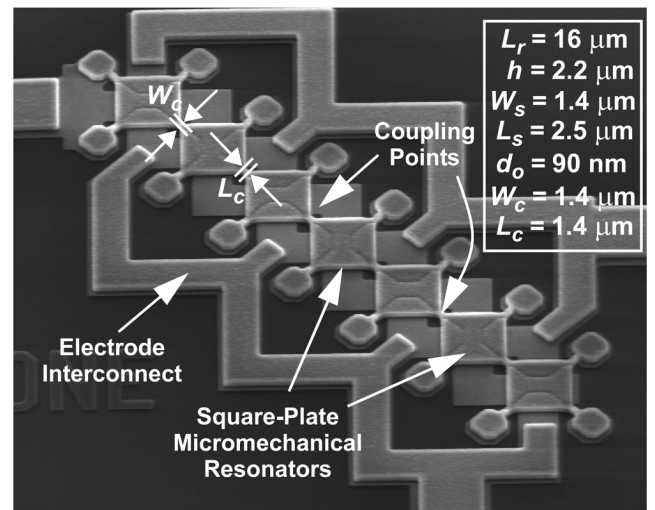Fig. 20. SEM of a 72-MHz corner-supported square plate μmechanical resonator.

Fig. 18. SEM of a 68-MHz center-stem square plate μmechanical resonator.

Fig. 21. SEM of a 72-MHz mechanically coupled array of seven corner-supported square plate resonators.

the purpose of comparing with the one-port resonator arrays to be described later. As will be explained in more detail later, the arrays were hooked up in one-port configurations rather than two-port for electrical routing convenience. Whether devices are hooked up as one- or two-ports has little impact on the overall enhancement factor afforded by arraying.

Fig. 23 presents the measured frequency spectrum for the corner-supported plate of Fig. 20, again under vacuum and using

Fig. 22. Frequency response characteristic for a 68.5-MHz center-stem square plate resonator.
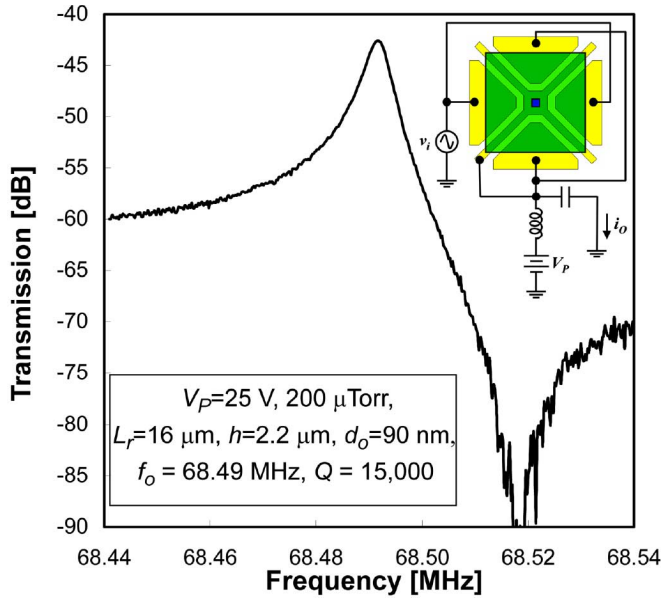

Fig. 23. Frequency response characteristic for a 71.7-MHz corner-support square plate resonator.

a one-port test setup, but this time with a much higher dc-bias of 40 V, which was not possible with the center-stem device due to pull-in limitations, but which is now permissible by a higher stiffness afforded by corner supports. The device has a Q of 17,500, which is higher than the center-stem resonator Q, showing that removal of a (potentially misaligned) center stem support does indeed improve the quality factor. The resonance frequency of the device is 71.7 MHz, which is greater than the frequency of the center-stem design, verifying the theory of Section IV, where added support stiffness is responsible for frequency increase. The measured R_x of the corner-supported device is 2.82 kΩ, which is much smaller than the 13.4 kΩ exhibited by the center-anchored device because a higher dc-bias voltage is used (permitted by its higher pull-in voltage). Table II presents a comparison of theoretical and measured resonance frequency and motional resistance values for center-anchor and corner-supported devices.

To assess the validity of (33), Fig. 24 presents a comparison of frequency versus support length plots predicted by (34) and measured for a corner-supported square plate resonator, showing a clear increase in the resonance frequency with decreasing support beam length. The slight deviation of the theory from measurement for short support beams comes about because (33) neglects the mass and stiffness of the small portion of the coupling beam at the plate corner. (See the definition of L_S in Fig. 7.) At the frequency of these devices, the beam length corresponding to half of a quarter wavelength ($\lambda/8$) is around 8 μm and the prediction by (34) loses its accuracy for beams longer than this value due to its short beam assumption ($L_S < \lambda/8$), which explains the slight deviation between theory and measurement for longer beams.

Fig. 25 presents a plot of measured quality factor versus support beam length for a 68.5-MHz corner-supported square plate resonator. The Q decreases rapidly below 20,000 for support beams shorter than 2.5 μm and it is almost constant
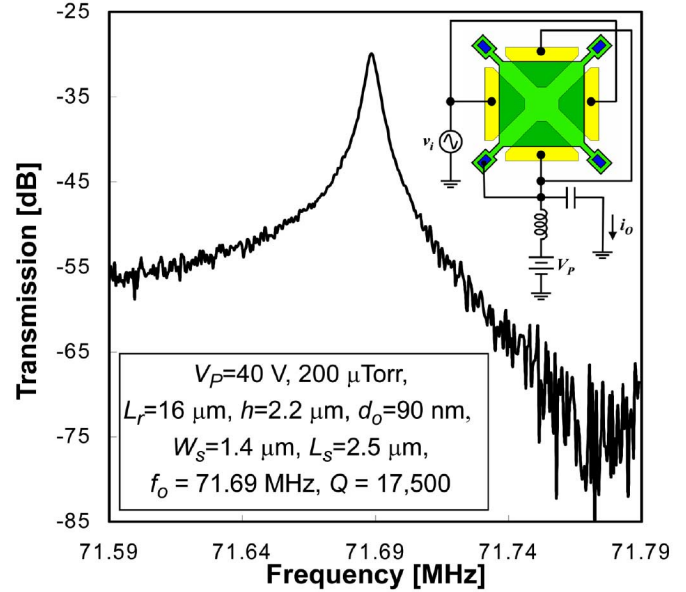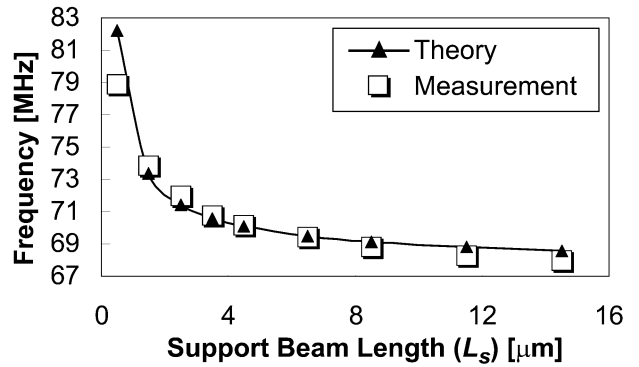

Fig. 24. Comparison of frequency (f_{oS}) versus support length (L_s) plots for a corner-support square resonator obtained by (34) and by measurement.

around 30,000 for beams longer than 4.5 μm. Although there was no measured Q data for the case of quarter-wavelength beam length $L_s = 15.7$ μm, the catastrophic pull-in voltage for a square resonator with quarter wavelength supports is calculated to be approximately 15 V, which is much lower than the 40 V pull-in voltage of the resonator with 4.5 μm supports. Given that devices with 4.5 μm support beams can sustain much higher dc-bias voltages without pulling in and still retain fairly high Q's around 30,000, they can potentially achieve much smaller R_x. This encourages the use of 4.5 μm support beam lengths in future designs to maximize both Q and pull-down voltage. This measurement also shows that corner-supported square plates exhibit almost 2X larger Q's compared to center-anchored square plates, as well as free-free beam micromechanical resonators [17], at the same frequency.

B. Mechanically-Coupled Resonator Arrays

Fig. 26 presents frequency characteristics measured using two-port configurations under vacuum for a stand-alone center-stem device, and three-, five-, and eleven-resonator
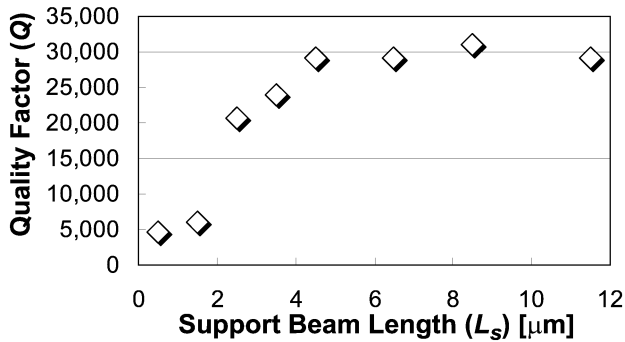
Fig. 25. Measured quality factor (Q) versus support length (L_s) plot for a 68.5-MHz corner-supported square resonator.
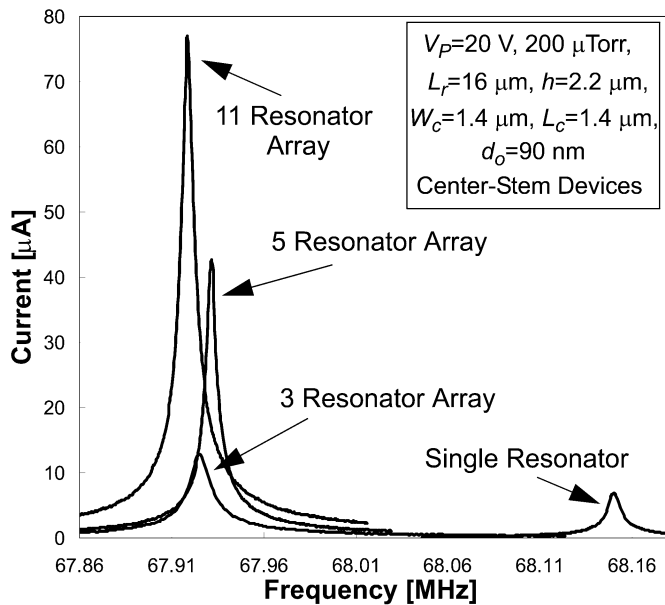

Fig. 26. Frequency response spectra for a 68-MHz stand-alone center-stem resonator and coupled center-stem square resonator arrays with three, five, and eleven resonators.

TABLE III
68-MHz CENTER-STEM SQUARE RESONATOR ARRAY PERFORMANCE

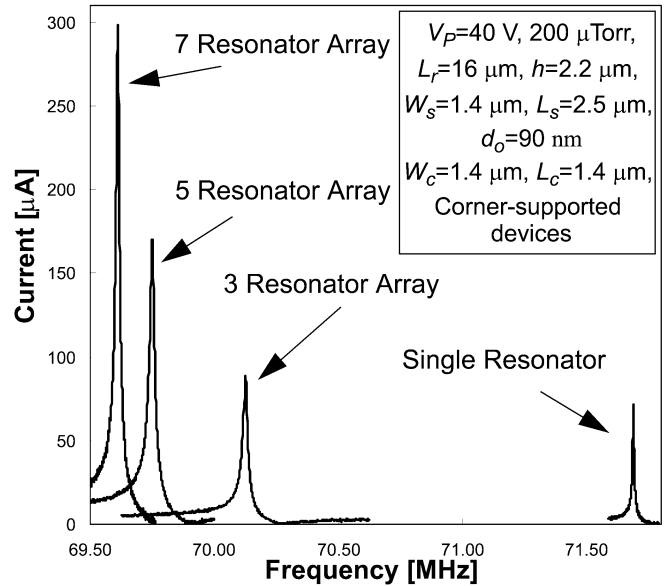| No. of Resonators	Measured R_x [kΩ]	R_x Reduction Factor	Q-Normalized R_x Reduction Factor	Measured Q
1	32.3	1X	1X	10,500
3	17.3	1.9X	3.2X	6,200
5	5.1	6.3X	5.3X	12,400
11	2.8	11.5X	10.7X	11,300

Fig. 27. Frequency response spectra for a 72-MHz stand-alone corner-supported resonator and coupled corner-supported square resonator arrays with three, five and seven resonators.

TABLE IV
72-MHz CORNER-SUPPORTED SQUARE RESONATOR ARRAY PERFORMANCE

No. of Resonators	Measured R_x [kΩ]	R_x Reduction Factor	Measured Q
1	2.82	1X	17,500
3	2.30	1.2X	5,900
5	1.06	2.7X	8,900
7	0.48	5.9X	9,100

center-stem coupled array devices with peak heights clearly increasing with the number of resonators coupled. To allow for direct comparison of motional resistances, the same dc-bias was applied to each device for measurement, and a low ac drive level (less than 5 mV) was used to avoid nonlinearity. Table III presents a comparison of R_x values for each of these devices, clearly showing decreases in R_x with increases in the number of resonators used. Note that the deviations in the Q seen in Table III for the arrays versus the single-resonator are partly responsible for R_x reduction factors that are not exactly equal to the number of resonators. For a fair comparison, Table III also includes reduction factors in Q-normalized R_x values (normalized by multiplying R_x of each resonator by its Q). The Q-normalized R_x reduction factors of 3.2X, 5.3X, and 10.7X, exhibited by three-, five- and eleven-resonator mechanically-coupled resonator arrays, respectively, verify the equivalence between reduction factor and number of resonators predicted by (35). The Q of the array is dominated by the lowest Q resonator (i.e., if one of the constituent resonators of the array has low Q, this lowers the Q of the array).

Fig. 27 presents frequency characteristics measured using a one-port configuration under vacuum for corner-supported devices, including a stand-alone device (i.e., device of Fig. 20), and three-, five- and seven-resonator coupled array devices. Note that when forming the coupled arrays of corner-supported square plates, the supports at the coupling points were removed and replaced by coupling stubs. Table IV presents a comparison of R_x values for each of these devices, again showing decreases in R_x with increases in the number of resonators used. For the three-resonator array, there is very little reduction in R_x, mainly due to a dramatic decrease in Q. As the array size becomes larger, however, the Q rises, and the R_x reduction factor seems to approach the expected value equal to the number of resonators in the array.
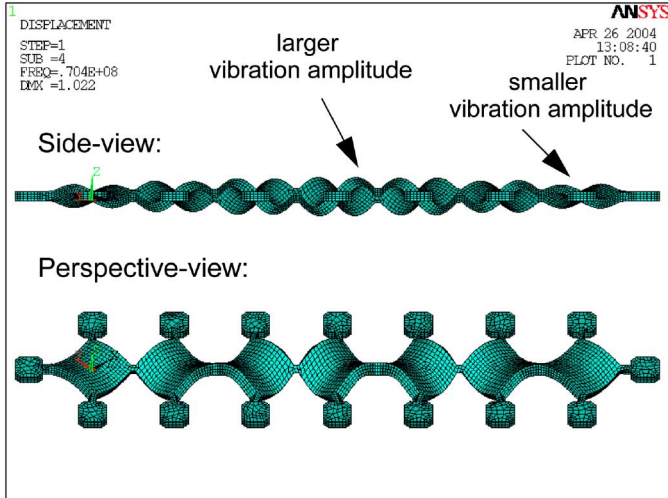
Fig. 28. Vibration mode shape of a seven-resonator array of square plates supported by torsional beams at corners as simulated via ANSYS.

Fig. 29. Measured frequency spectrum verifying suppression of the higher frequency filter modes by choice electrode excitation.

Part of the reason for the observed improvement in Q with increasing array size is the reduction in the number of supports per resonator, i.e., an increase in the number of resonators with only two corner supports. In particular, the resonators at the two ends of the array have three supports, and thus, more paths through which energy can be lost to the substrate (i.e., more anchor dissipation) and higher stiffness compared to the inner resonators with only two supports. Since the three resonator array has two three-support resonators and only one two-port one, its performance is governed more by three-support resonators, which contributes to its lower overall Q. Larger arrays, on the other hand, are dominated by two-support resonators, giving rise to an improvement in the quality factor. By eliminating third anchors at the two ends of the array, higher Q should be achievable in future designs.

In addition to higher Q, larger arrays of the corner-supported type also provide larger vibration amplitudes compared to smaller arrays. In particular, since the mechanical stiffness is smaller for the inner resonators, the vibration amplitude becomes larger closer to the center of a large array, as seen in Fig. 28, which presents the ANSYS simulated vibration mode-shape of a corner-supported seven-resonator array. This results in further increases in the resonator array output, which explains why R_x is still reduced 5.9X despite the Q degradation by a factor of 0.5 (relative to a single resonator) in the seven-resonator array. The seven-resonator array of Fig. 21 has a motional resistance of 480 Ω, which is the lowest R_x demonstrated to date for any capacitively actuated micromechanical resonator at this frequency.

As expected from Section V, and as seen in Figs. 26 and 27, in addition to lowering R_x, mechanical coupling of resonators also shifts the center frequency of the peak from that of a stand-alone resonator. For the arrays of Fig. 26, the frequency shift is less than 0.02% and can be fixed by merely adjusting the applied dc-bias voltage V_P to constituent resonators. Note that the measured center frequency of the five-resonator array is larger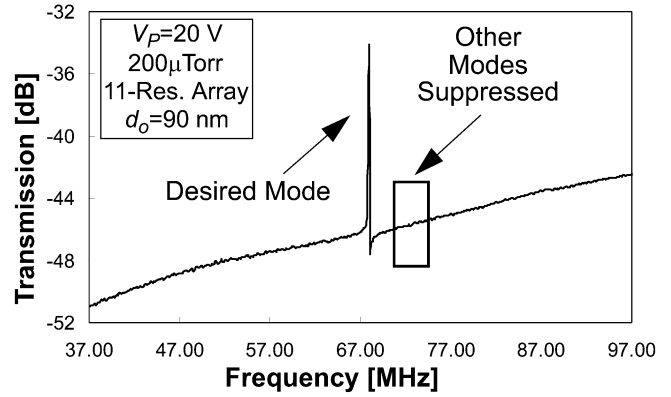 than that of the 3-resonator array, and this does not agree with theory. In particular, theory predicts the opposite for the fundamental mode (used here) of any given array. In particular, theory expects the fundamental-mode frequency to decrease as the number of resonators used in the array increases, since the ratio of fundamental-mode array stiffness to array mass decreases as the number of resonators increases. This comes about because in the fundamental mode, the resonators move in such a way that their couplers do not flex [20], as clearly illustrated in the first mode depiction in Fig. 13 for the case of a three-resonator array. When couplers do not flex, they add mass to the system without adding stiffness, thereby decreasing the array stiffness-to-mass ratio and in turn decreasing the overall array frequency according to (33). The fact that the measured center frequency of the five-resonator array of center-stem-supported resonators is larger than that of the three-resonator array is likely caused by finite fabrication tolerances, which are significant here, since the peaks for the center-stem-supported resonator arrays are so close together.

The corner-supported resonator arrays, on the other hand, show measured performance more in line with theoretical prediciton, with frequency decreasing as the number of resonators in the array increases. From Fig. 27, the frequency shifts are seen to be significant enough that the mechanical design of the array should be adjusted if the array mode frequency is intended to match that of the original stand-alone resonator.

C. No Spurious Modes

To ascertain how effectively the unwanted modes in the mechanically coupled array have been suppressed via strategic electrode phasing, Fig. 29 presents the spectrum for a coupled array of eleven center-stemmed square resonators measured over a wide frequency range. The existence of only a single peak verifies that only the first filter mode is excited, while the higher modes expected up to eleventh mode at 73.8 MHz (as determined by ANSYS), have been effectively suppressed.

D. Linearity

To assess the linearity of the array method, Fig. 30 presents measured plots of output power P_o vs. input power P_i for the single corner-supported square plate microresonator of Fig. 20 and array of five of them. In these plots, the $P_{o,\mathrm{fund}}$ curves were obtained by driving the resonator or array in question by an
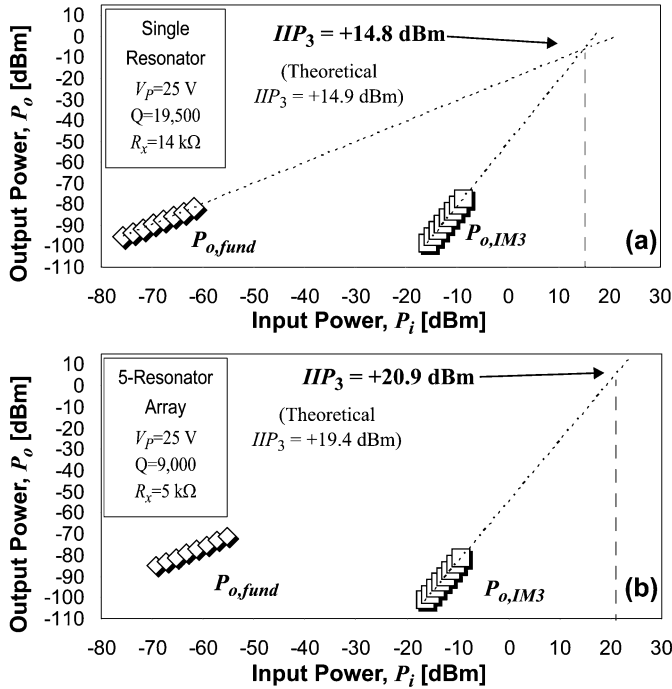
Fig. 30. Measured plots of output power P_o versus input power P_i for (a) the single corner-supported square plate microresonator of Fig. 20 and (b) an array of five of them, showing extrapolated IIP_3's of $+14.8$ dBm and $+20.9$ dBm, respectively.

input signal at its resonance frequency f_o with a power level indicated by the x-axis. The $P_{o,IM3}$ curves, on the other hand, were obtained using the so-called "two-tone test" [10], where out-of-band input signals at $f_o + \Delta f$ and $f_o + 2\Delta f$, with $\Delta f = 200$ kHz, were applied to the resonator or array input with equal powers governed by the x-axis, and the output signal taken at f_o. (All consistent with the descriptions in Section III.) As shown, the single resonator exhibits an R_x of 14 kΩ and an extrapolated IIP_3 of $+14.8$ dBm, which is quite close to the theoretical prediction of $+14.9$ dBm using (20). The array of five mechanically coupled resonators exhibits a lower R_x of 5 kΩ and a 9.7 dB higher IIP_3 of $+20.9$ dBm, verifying significantly better array linearity, and again matching the $+19.4$ dBm theoretical prediciton of (20). Thus, the described mechanically coupled resonator arraying technique does indeed reduce R_x without degrading device linearity, and in fact improves linearity, as predicted by the theory of Section III.

E. Temperature Dependence

Fig. 31 presents a plot comparing frequency versus temperature measurements for a 63-MHz stand alone center-anchored square resonator and a coupled array of five of them. The extracted TC_f's (temperature coefficients of frequency) of the stand-alone resonator and the coupled array are -10.5 ppm$/°$C and -12.8 ppm$/°$C, respectively, where the thermal stability of the resonator array is seen to be only slightly worse than the stand-alone resonator. This is somewhat reasonable, since the single square plate is smaller and anchored to the substrate only at a single point, while the array is both larger and anchored at several locations, making it more susceptible to structure-to-substrate thermal expansion mismatches. Both
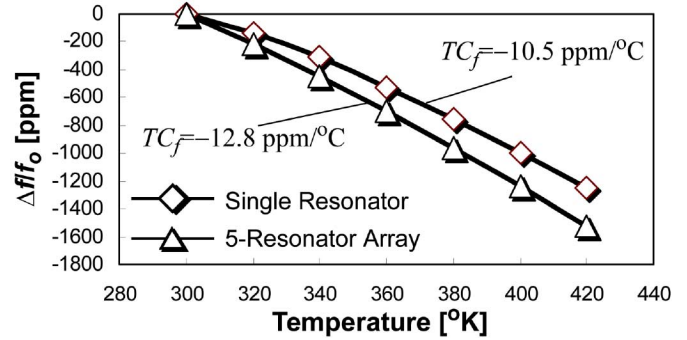

Fig. 31. Measured frequency versus temperature plots for a 63-MHz single center-anchor square resonator and an array of five of them.
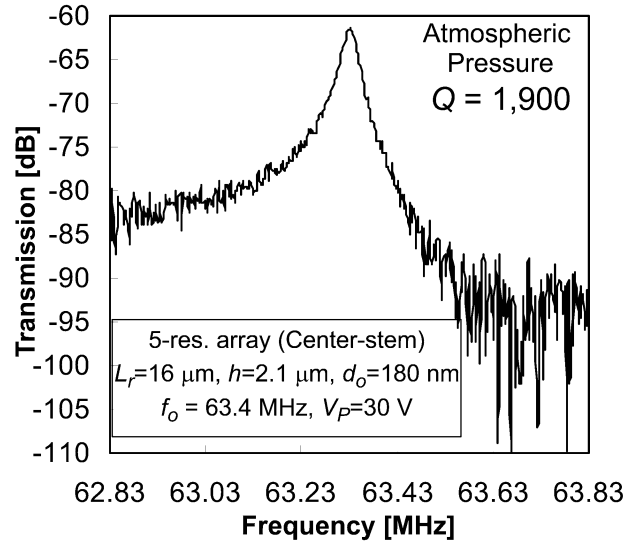

Fig. 32. Frequency characteristic for a 63-MHz five resonator coupled center-stem square resonator array measured under atmospheric pressure.

thermal dependences are on par or better than that measured for previous uncompensated free-free beam micromechanical resonators [17], [25].

F. Operation Under Atmospheric Pressure

Up to this point, all of the measured curves shown in this paper were done under 200 μTorr vacuum, with the intent of eliminating viscous gas damping so as to better ascertain the degree to which design-related loss mechanisms, such as anchor or material losses, govern the Q of the more complex array structure. However, due their high stiffness, the square plate resonators of this work operate with internal energies per cycle much higher than the energy losses per cycle caused by viscous gas damping. As such, the resonators and arrays of this work actually do not require vacuum to attain reasonably high Q's [27]. To illustrate, Fig. 32 presents the frequency characteristic for a five resonator array of 63-MHz center-anchor square plate micromechanical resonators measured under atmospheric pressure, yet still showing a Q of 1,900, which is still sufficient for use in many IF communication applications. This removal of the requirement for vacuum for stiff micron-scale (as opposed to nano-scale) micromechanical resonators has enormous implications, as it allows a substantial reduction in the manufacturing

cost of such devices, as well as increases their reliability and lifetime in commercial applications.

G. Conclusions

Mechanically coupled parallel resonator arrays with combined output currents have been demonstrated with series motional resistances smaller than that of a single resonator by factors equal to the number of resonators used in the array. The method demonstrated is also superior to mere combining of responses from separate resonators, since by mechanically coupling resonators, it automatically generates a single resonance response (i.e., mode) from all resonators, without the need for absolute matching of individual resonator responses. Although this paper has focused mainly on lowering resonator impedances, another direct benefit of this approach is a substantial enhancement of the power handling capability of the combined device which is important for micromechanical resonator oscillators and front-end filters, alike. As such, this technique solves many of the remaining issues that presently slow the insertion of vibrating micromechanical resonator devices into practical communication systems, and thus, helps clear a path towards the fully integrated communication systems targeted by vibrating RF MEMS technology.

REFERENCES

[1] J. Wang, J. E. Butler, T. Feygelson, and C. T.-C. Nguyen, "1.51-GHz nanocrystalline diamond micromechanical disk resonator with material-mismatched isolating support," in *Tech. Digest, 17th Int. IEEE MEMS Conf.*, Maastricht, The Netherlands, Jan. 25–29, 2004, pp. 641–644.

[2] C. T.-C. Nguyen, "Vibrating RF MEMS for next generation wireless applications," in *Proc. 2004 IEEE Custom Integrated Circuits Conf.*, Orlando, FL, Oct. 3–6, 2004, pp. 257–264.

[3] H. A. C. Tilmans, W. D. Raedt, and E. Beyne, "MEMS for wireless communications: 'From RF-MEMS components to RF-MEMS-SiP," *J. Micromech. Microeng.*, vol. 13, no. 4, pp. S139–S163, Jul. 2003.

[4] B. Bircumshaw, G. Lui, H. Takeuchi, T.-J. King, R. T. Howe, O. O'Reilly, and A. P. Pisano, "The radial bulk annular res.: Towards a 50 ω MEMS filter," in *Dig. Tech. Papers, Transducers'03*, Boston, MA, Jun. 8–12, 2003, pp. 875–878.

[5] S. Pourkamali and F. Ayazi, "SOI based HF and VHF single-crystal silicon resonators with sub-100 nanometer vertical capacitive gaps," in *Tech. Digest, 12th Int. Conf. Solid-State Sensors, Actuators, and Microsystems (Transducers'03)*, Jun. 2–6, 2003, pp. 837–840.

[6] C. T.-C. Nguyen, "Transceiver front-end architectures using vibrating micromechanical signal processors," in *Dig. Papers, Topical Mtg. Silicon Monolithic IC's in RF Systems*, Sep. 12–14, 2001, pp. 23–32.

[7] F. D. Bannon, III, J. R. Clark, and C. T.-C. Nguyen, "High-Q HF microelectromechanical filters," *IEEE J. Solid-State Circuits*, vol. 35, no. 4, pp. 512–526, Apr. 2000.

[8] M. U. Demirci, M. A. Abdelmoneum, and C. T.-C. Nguyen, "Mechanically corner-coupled square microresonator array for reduced series motional resistance," in *Tech. Digest, 12th Int. Conf. Solid-State Sensors, Actuators, and Microsystems (Transducers'03)*, Jun. 2–6, 2003, pp. 955–958.

[9] B. Razavi, *RF Microelectronics*. Upper Saddle River, NJ: Prentice-Hall, 1998.

[10] R. Navid, J. R. Clark, M. Demirci, and C. T.-C. Nguyen, "Third-order intermodulation distortion in capacitively-driven CC-beam micromechanical resonators," in *Tech. Digest, IEEE MEMS Conf.*, Interlaken, Switzerland, Jan. 21–25, 2001, pp. 228–231.

[11] S. Timoshenko, *Vibration Problems in Engineering*, 4 ed. New York: Wiley, 1974.

[12] H. A. C. Tilmans and R. Legtenberg, "Electrostatically driven vacuum-encapsulated polysilicon resonators: Part II. Theory and performance," *Sens. Actuators A, Phys.*, vol. A45, pp. 67–84, 1994.

[13] R. A. Johnson, *Mechanical Filters in Electronics*. New York: Wiley, 1983.

[14] R. D. Blevins, *Formulas for Natural Frequency and Mode Shape*. Malabar, FL: Krieger, 1984.

[15] C. T.-C. Nguyen and R. T. Howe, "An integrated CMOS micromechanical resonator high-Q oscillator," *IEEE J. Solid-State Circuits*, vol. 34, no. 4, pp. 440–455, Apr. 1999.

[16] Y.-W. Lin, S. Lee, Li S.-S, Y. Xie, Z. Ren, and C. T.-C. Nguyen, in *Dig. Tech. Papers, 2004 IEEE Int. Solid-State Circuits Conf.*, 2003, vol. 47, pp. 322–323.

[17] K. Wang, A.-C. Wong, and C. T.-C. Nguyen, "VHF free-free beam high-Q micromechanical resonators," *J. Microelectromech. Syst*, vol. 8, no. 4, pp. 534–557, Dec. 1999.

[18] H. Nathanson, W. E. Newell, R. A. Wickstrom, and J. R. Davis, Jr, "The resonant gate transistor," *IEEE Trans. Electron Devices*, vol. ED-14, no. 1, pp. 117–133, Mar. 1967.

[19] S. Timoshenko, *Strength of Materials, Part I: Elementary Theory and Problems*, 3rd ed ed. Melbourne, FL: Krieger, 1958.

[20] K. Wang and C. T.-C. Nguyen, "High-order medium frequency micromechanical electronic filters," *J. Microelectromech. Syst.*, vol. 8, no. 4, pp. 534–557, Dec. 1999.

[21] D. S. Greywall and P. S. Busch, "Coupled micromechanical drumhead resonators with practical application as electromechanical bandpass filters," *J. Micromech. Microeng.*, vol. 12, no. 6, pp. 925–938, Nov. 2002.

[22] M. P. Castanier and C. Pierre, "Individual and interactive mechanisms for localization and dissipation in a mono-coupled nearly-periodic structure," *J. Sound Vibrat.*, vol. 168, no. 3, pp. 479–505, Dec. 1993.

[23] H. Guckel, D. W. Burns, H. A. C. Tilmans, D. W. DeRoo, and C. Rutigliano, "The mechanical properties of fine-grained polysilicon: The repeatability issue," in *Proc. IEEE Solid-State Sens. Actuator Workshop Tech. Dig*, Hilton Head, SC, Jun. 1998, pp. 96–99.

[24] W. E. Newell, "Miniaturization of tuning forks," *Science*, vol. 161, pp. 1320–1326, Sep. 1968.

[25] M. U. Demirci and C. T.-C. Nguyen, "Higher-Mode free-free beam micromechanical resonators," in *Proc. Annu. IEEE Int. Frequency Control Symp.*, Tampa, FL, May 5–8, 2003, pp. 810–818.

[26] J. R. Clark, W.-T. Hsu, and C. T.-C. Nguyen, "Measurement techniques for capacitively-transduced VHF-to-UHF micromechanical resonators," in *Dig. Technical Papers, 11th Int. Conf. Solid-State Sensors Actuators*, pp. 1118–1121.

[27] J. Wang, Z. Ren, and C. T.-C. Nguyen, "Self-aligned 1.14-GHz vibrating radial-mode disk resonators," in *Tech. Digest, 12th Int. Conf. Solid-State Sensors, Actuators, and Microsystems (Transducers'03)*, Jun. 2–6, 2003, pp. 947–950.

Mustafa U. Demirci (S'98–M'06) received the B.S. degree in electrical and electronics engineering from Middle East Technical University, Ankara, Turkey, in 1997, and the M.S. and Ph.D. degrees in electrical engineering from the University of Michigan, Ann Arbor, in 1999 and 2005, respectively. His Ph.D. research involved integrated circuit technology and microelectromechanical systems for communications.

In 2005, he joined Toyota Technical Center, Ann Arbor, MI, where he is currently a Senior Research Scientist.

Dr. Demirci was a recipient of the Turkish Scientific and Technical Research Council (TUBITAK) NATO-A1 scholarship in 1997.

Clark T.-C. Nguyen (S'90–M'95–SM'01) received the B. S., M. S., and Ph.D. degrees from the University of California, Berkeley, in 1989, 1991, and 1994, respectively, all in electrical engineering and computer sciences.

In 1995, he joined the faculty of the University of Michigan, Ann Arbor, where he was a Professor in the Department of Electrical Engineering and Computer Science until mid-2006. In 2006, he joined the Department of Electrical Engineering and Computer Sciences at the University of California, Berkeley,

where he is currently a Professor and a Director of the Berkeley Sensor and Actuator Center. His research interests focus upon microelectromechanical systems (MEMS) and include integrated micromechanical signal processors and sensors, merged circuit/micromechanical technologies, RF communication architectures, and integrated circuit design and technology. From 1995 to 1997, he was a member of the National Aeronautics and Space Administration (NASA)'s New Millennium Integrated Product Development Team on Communications, which roadmapped future communications technologies for NASA use into the turn of the century. In 2001, he founded Discera, Inc., a company aimed at commercializing communication products based upon MEMS technology, with an initial focus on the very vibrating micromechanical resonators pioneered by his research in past years. He served as Vice President and Chief Technology Officer (CTO) of Discera until mid-2002, at which point he joined the Defense Advanced Research Projects Agency (DARPA) on an IPA, where he served for 3 1/2 years as the Program Manager of the MEMS, Micro Power Generation (MPG), Chip-Scale Atomic Clock (CSAC), MEMS Exchange (MX), Harsh Environment Robust Micromechanical Technology (HERMIT), Micro Gas Analyzers (MGA), Radio Isotope Micropower Sources (RIMS), RF MEMS Improvement (RFMIP), Navigation-Grade Integrated Micro Gyroscopes (NGIMG), and Micro Cryogenic Coolers (MCC) programs, in the Microsystems Technology Office of DARPA.

Prof. Nguyen received the 1938E Award for Research and Teaching Excellence from the University of Michigan in 1998, an EECS Departmental Achievement Award in 1999, the Ruth and Joel Spira Award for Teaching Excellence in 2000, and the University of Michigan's 2001 Henry Russel Award. He recently received the Cady Award from the 2006 IEEE Frequency Control Symposium. Among his publication accolades are the Jack Raper Award from 2005 IEEE International Solid-State Circuits Conference, the 2004 DARPA Best Technical Presentation Award, the Best Invited Paper Award at the 2004 IEEE Custom Integrated Circuits Conference, and together with his students, the Best Student Paper Award in Category 1 at the 2005 Joint IEEE Frequency Control/Precise Time and Timing Interval (PTTI) Symposium, the Best Student Paper Award in the Frequency Control Category at the 2004 IEEE Ultrasonics, Ferroelectrics, and Frequency Control Symposium, and the Roger A. Haken Best Student Paper Awards at the 1998 and 2003 IEEE International Electron Devices Meetings. To date, he has organized and chaired a total of 35 IEEE and DARPA workshops.